2005-07-08

An Improved Flexible Neutron Detector For Powder Diffraction Experiments

Thomas Kevin McKnight
Brigham Young University - Provo

AN IMPROVED FLEXIBLE NEUTRON DETECTOR FOR POWDER DIFFRACTION EXPERIMENTS

by

Thomas K. McKnight

A thesis submitted to the faculty of

Brigham Young University

in partial fulfillment of the requirements for the degree of

Master of Science

Department of Physics and Astronomy

Brigham Young University

August 2005

BRIGHAM YOUNG UNIVERSITY

GRADUATE COMMITTEE APPROVAL

of a thesis submitted by

Thomas K. McKnight

This thesis has been read by each member of the following graduate committee and by majority vote has been found to be satisfactory.

_____	_____
Date	Branton Campbell, Chair
_____	_____
Date	J. Bart Czirr
_____	_____
Date	Lawrence B. Rees
_____	_____
Date	Steven E. Jones

BRIGHAM YOUNG UNIVERSITY

As chair of the candidate's graduate committee, I have read the dissertation of Thomas K. McKnight in its final form and have found that (1) its format, citations, and bibliographical style are consistent and acceptable and fulfill university and department requirements; (2) its illustrative materials including figures, tables, and charts are in place; and (3) the final manuscript is satisfactory to the graduate committee and is ready for submission to the university library.

_____ _____

Date Branton Campbell
Chair, Graduate Committee

Accepted for the Department

_____

Ross L. Spencer
Graduate Coordinator

Accepted for the College

_____

G. Rex Bryce
Associate Dean, College of Physical
and Mathematical Sciences

ABSTRACT

AN IMPROVED FLEXIBLE NEUTRON DETECTOR FOR POWDER DIFFRACTION EXPERIMENTS

Thomas K. McKnight

Department of Physics and Astronomy

Master of Science

Large amounts of money are being applied to the construction of the next generation of spallation sources for neutron scattering. Neutron powder diffraction instruments will be an important element of these facilities and the incorporation of detectors into these instruments with a high neutron capture efficiency is desirable.

A new detector design named the Flexible Embedded Fiber Detector (FEFD) has been developed and tested for this thesis. This detector is based on wavelength shifting fibers embedded in a zinc-sulfide lithium-fluoride based scintillator. The virtue of this design is that the detecting surface can be curved around the Debye-Scherrer rings. This virtue is lacking in other detector designs, making them more complex and poorer in performance than our FEFD detectors.

Monte Carlo calculations were performed to determine the neutron capture efficiencies of our FEFD detectors, which proved to be much higher than those of the

proposed powder diffractometer design for the Spallation Neutron Source and about equal with the efficiency for the ISIS powder diffractometer design. Four FEFD detector prototypes were then fabricated and tested at the Intense Pulsed Neutron Source at Argonne National Laboratory. We find that our measured and calculated relative efficiencies are in good agreement.

ACKNOWLEDGMENTS

My wife, Alissa, has exercised extreme patience while I have been enrolled in the Master's program and also attended to work and other responsibilities. During that time she has given birth to two children and provided the nurturing they needed while my attention was diverted to these responsibilities.

Bart Czirr has provided tremendous technical support and learning opportunities. This thesis would be lacking in many areas if it were not for his expertise. In the same breath, Branton Campbell provided direction and inspired me to think more thoroughly before proposing ideas; traits that will prove valuable throughout life.

Wesley Lifferth machined the molds needed to fabricate my detectors. He did so in a professional manner and often in short notice with a smile on his face.

My visit to IPNS could not have been a better experience. The staff was accommodating and always willing to help. My thanks goes to Kenneth Littrell who oversees the CHEX instrument. He was willing to help on a moments notice.

Finally, Bicron provided the wavelength-shifting fiber samples. When my stocks were low, Robin Wascovich took the initiative to locate and send more fibers.

TABLE OF CONTENTS

LIST OF TABLES

LIST OF FIGURES

Chapter 1

Introduction and Background

1.1 – Importance of Neutron Diffraction

Throughout the twentieth century, many tools have been developed for investigating structure-property relationships in materials. Among the important probes of atomic and molecular structure, neutron scattering has been instrumental in developing new superconductors, polymers, pharmaceutical products and a long list of other materials.

The basic purpose of neutron scattering is to gather information about the material properties of a sample. This is done by analyzing the scattering that an incident beam of neutrons undergoes after interacting with a sample. Since neutrons are subatomic particles, they can be described in terms of their quantum mechanical de Broglie wavelength given by the relation $\lambda = h/mv$, which implies that a neutron beam can be tuned to a particular wavelength simply by allowing a selected velocity of neutrons.

The form of neutron scattering used to probe a material depends on the characteristics of a particular sample. When the sample is of a crystalline form, where atoms are placed at equivalent positions dictated by the lattice structure, a form of scattering known as diffraction occurs. In polycrystalline samples, the many crystal granules or domains require the use of powder diffraction as the probe [1]. These small crystals are most usually due to the limitations of the crystal growth or the environmental parameters of a sample during an experiment, such as extreme temperature and pressure,

which only allow for a powdered sample to exist. Powder diffraction has found uses for investigating the structure of magnetic materials, zeolites, ionic conductors, materials containing hydrogen and other light elements and many other materials.

For typical powder diffraction experiments the neutrons will be considered to be elastically diffracted and in the thermal energy range. Strictly speaking, a thermalized neutron is at thermal equilibrium with room temperature (293 K) which is at 0.0253eV. However, when used in the broader context of neutron scattering, thermal neutrons are considered to be of the order of 0.005 to 0.1 eV [2]. The term *elastic* scattering specifies that energy is not transferred from the sample to the neutron. This implies that the incident and final energies are equal in magnitude; that is, $E_i = E_f$.

1.2 – Present and Future Neutron Scattering Facilities

At this time there are several well-utilized neutron scattering facilities around the world. These facilities produce a neutron flux that is channeled down beamlines to different neutron scattering instruments. A typical facility may have 10-20 different beamlines with one or two of these devoted to neutron powder diffraction.

Two common sources exist for producing neutrons for scattering experiments, the nuclear reactor and the pulsed spallation source. While reactor sources have a higher average flux, a pulsed source naturally allows time-of-flight (TOF) separation of the neutron energy spectrum, an important advantage for certain types of experiments. The lack of a reactor also makes these facilities more politically attractive.

Historically, reactor sources were the earliest method of producing neutrons for scattering experiments. Currently, the most recognized and up-to-date facility that

employs a reactor source is the High Flux Reactor (HFR) at the Institute Laue Langevin in France which was commissioned in 1972.

Since the commissioning of HFR, the spallation technique has been introduced as an important alternative to reactors. This technique involves "spalling" or striking a nucleus with a high-energy incident particle to knock-out neutrons. Protons are used as the incident particles of choice due to the ease at which they may be produced and accelerated. The standard means of accelerating these protons is with a linear accelerator. These protons are then sent into a cyclotron from which they are released onto a target in pulses of 30, 50 or 60 hertz depending on the facility. When these protons spall neutrons from target nuclei, neutrons are emitted isotropically. Beamlines will then accept any of the neutrons that pass through their apertures and channel them to their respective instruments [3].

The first spallation source to go online was at Argonne National Laboratory in 1981 and is known as the Intense Pulsed Neutron Source (IPNS). This facility was followed in 1985 by the Los Alamos Neutron Science Center (LANSCE) at Los Alamos National Laboratory and ISIS at Rutherford Appleton Laboratory in Great Britain. ISIS is the current leader in flux production and the standard against which other facilities draw comparisons.

The demands of industry and research institutions for higher-caliber neutron scattering facilities has resulted in the present construction of the next generation of multi-billion dollar facilities, which include the Spallation Neutron Source (SNS) at Oak Ridge National Laboratory[4] and the Japanesse Spallation Neutron Source (JSNS) at the Japan Atomic Energy Research Institute[5]. SNS is anticipated to run with a neutron flux

29 times greater than that at ISIS while JSNS should have a flux that is 31 times greater [6]. Also, at a level comparable to ISIS, the Chinese Spallation Neutron Source (CSNS) has been proposed and is waiting funding approval [7].

1.3 – Scope of the Thesis

New spallation facilities aim to have the best-in-class instruments that their budgets will allow in accordance with the latest advances in detection technology. One of the most important considerations for powder diffraction detectors is that of neutron detection efficiency. A higher efficiency allows higher counting statistics in a given amount of time as well as shorter sample runs which allows more users to cycle through a facility. The fulfillment of such considerations would increase both the value and scientific impact of a detector.

The scope of this thesis is to model, test and evaluate four design configurations for a new neutron powder diffractometer module called the Flexible Embedded Fiber Detector (FEFD). In comparison with the other detector designs currently in use or under development, the FEFD design has a superior combination of neutron detection efficiency, simplicity, and cost. This detector involves the use of wavelength-shifting optical fiber embedded in a flexible zinc-sulfide lithium-fluoride (ZnS/LiF) thermal neutron scintillator. When thermal neutrons enter the ZnS/LiF scintillator, they may be captured by the ^{6}Li in the LiF leading to the production of scintillation photons in ZnS which are isotropically radiated. A portion of the scintillation photons are trapped in the wavelength-shifting fibers and transmitted down their lengths to be detected and analyzed.

Four proof-of-principle prototypes were constructed with differing fiber sizes and shapes but with the same ZnS/LiF composition. Geometrically, two had round fibers and the other two had square fibers. As to the fiber width, two were 1 mm and the other two were 2 mm. Each prototype contained 3 fibers which were surrounded on all sides by no less than 0.5 mm of ZnS/LiF so that the inter-fiber separation was 1 mm within the ZnS/LiF matrix.

1.4 – Significance of the Research

The high efficiency, simplicity and low cost of a FEFD would make a facility that uses this detector more profitable and valuable. With the commissioning of new facilities and older facilities upgrading their detectors, the FEFD detectors have the potential for wide-scale use.

1.5 – Thesis Organization

Chapter 2 will give a brief overview of the principles of powder neutron diffraction. The principles of the Zns/LiF scintillator and wavelength-shifting fibers, which are important elements in this thesis, will be discussed in Chapter 3. To demonstrate the significance of the FEFD design, Chapter 4 will be devoted to explaining the current design used at ISIS and the proposed design for SNS, as well as their shortcomings. With the need for an improved design motivated, Chapter 5 will be describe the FEFD design and outline its benefits. Chapter 6 will explain some of the technical issues involved with the fabrication of the FEFD prototype modules. In Chapter 7 Monte Carlo computer calculations are made to compare the ^{6}Li neutron capture efficiency of each FEFD

detector. Measurements taken at the Intense Pulsed Neutron Source at Argonne National Laboratory add to the validity of these calculations and are discussed in Chapter 8. Some final conclusions and recommendations are made in Chapter 9.

Chapter 2

Powder Diffraction Geometry

2.1 - The Ewald Construction

An important and insightful construct for understanding neutron diffraction is that of the Ewald sphere. Consider a single crystal which contains many reciprocal lattice points as shown in the upper image of Figure 2.1. The incident and final wave vectors, $\mathbf{k}_i$ and $\mathbf{k}_f$, of equal magnitude $k = 2\pi/\lambda$ are represented, and both point to the surface of the Ewald sphere, where λ is the neutron wavelength. The reciprocal-space vector $\mathbf{Q} = \mathbf{k}_f - \mathbf{k}_i$ indicates the momentum transfer experienced by the scattered neutron. Using the upper illustration of Figure 12.1, one may geometrically determine that $Q = 2k\sin(\theta)$. Combined with the definition of d-spacing, $Q = 2\pi/d$, Bragg's law follows as $2d\sin\theta = \lambda$. The set of points on the surface of the Ewald sphere satisfy Bragg's law, and any reciprocal lattice vector that can be rotated onto this surface will give rise to a diffracted beam, also known as a Bragg reflection, at scattering angle 2θ as shown in Figure 2.1.

Powder diffraction in its basic form is easily understood in terms of the Ewald construction as follows. A powder sample contains a large number of crystal grains of the same material, each possessing its own reciprocal lattice. These reciprocal lattices are randomly oriented due to the random orientation of the powder grains which makes the locations of equivalent lattice points from different grains vary by a rotation around the

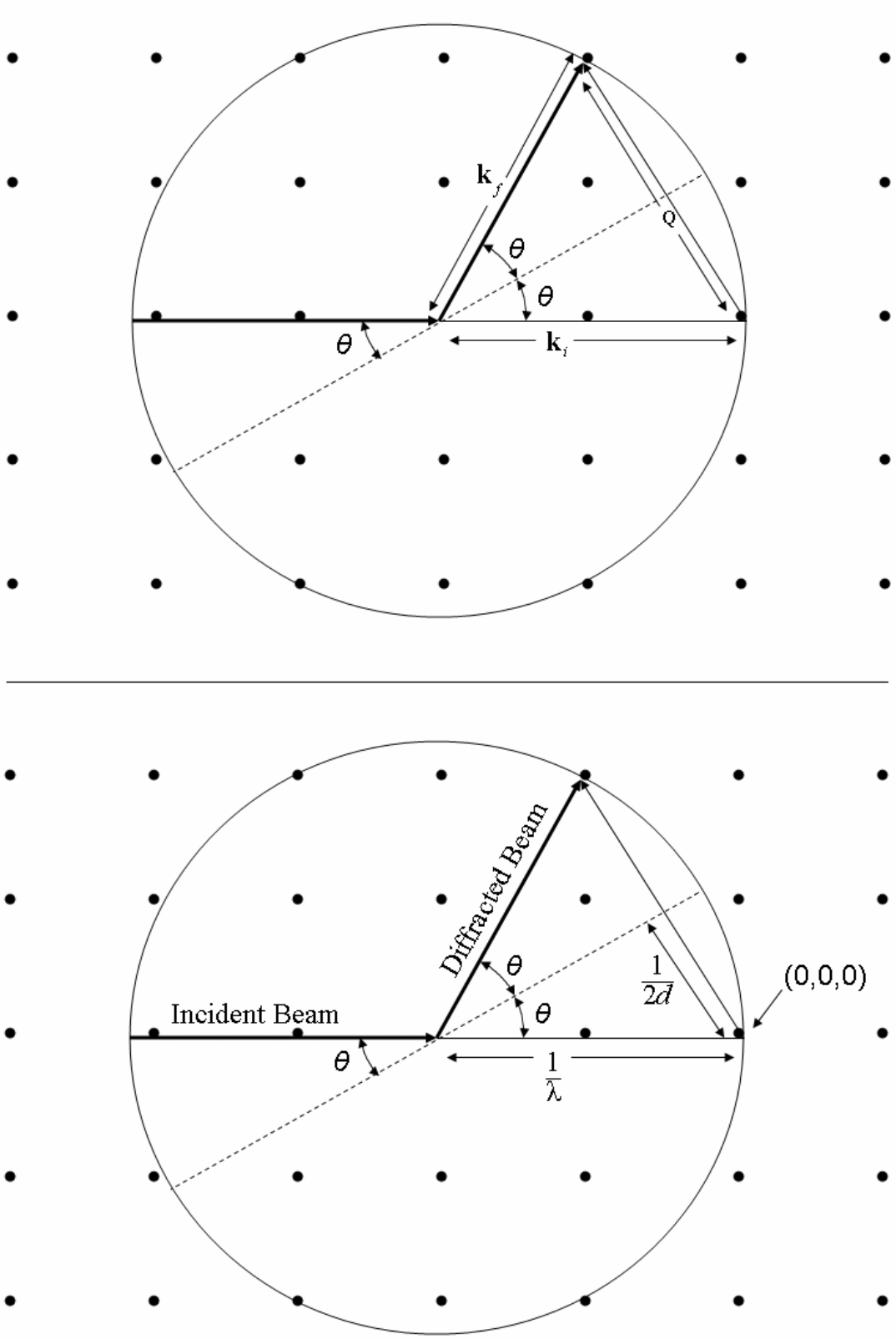

Figure 2.1 – The upper illustration shows an Ewald sphere in reciprocal space containing arbitrary vectors. The lower illustration shows an illustration of an Ewald sphere with vectors satisfying Braggs Law.

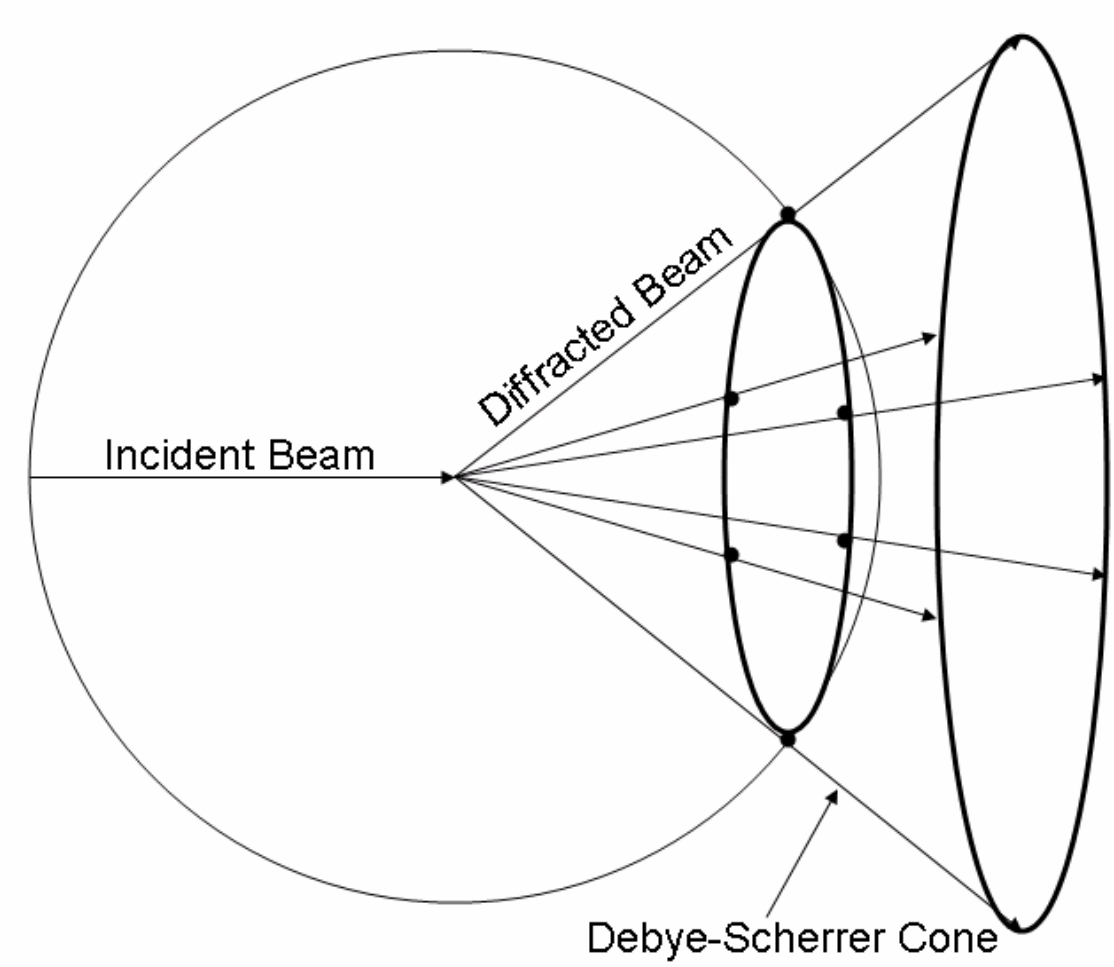

Figure 2.2 – In this image, the powder sample is imagined to be at the center of the Ewald Sphere. Incident neutrons are diffracted from this sample into a cone known as a Debye-Scherrer cone. This cone is centered around the axis of the incident neutron beam.

incident beam. This has the effect of tracing a circle on the surface of the Ewald sphere that is concentric with the axis of the incident neutrons as is evident in Figure 2.2. In physical terms, when a beam of neutrons passes through a powdered sample, a cone of diffracted neutrons will be produced, known as a Debye-Scherrer cone. When a flat detector intersects the Debye-Scherrer cone perpendicular to its axis, a Debye-Scherrer ring is formed [8]. In more general detector orientations, the detector image will be a general conic section, typically a hyperbola.

Chapter 3

Zinc Sulfide Scitillator and Wavelength-shifting Fiber Use in Powder Diffaction

3.1 – Definition and Importance of Scintillators

Two types of modern neutron detectors produce electrical signals which can be analyzed to give precise and immediate results and are commonly used for detecting low energy neutrons on the order of λ=1Å in diffraction experiments. One type is gas filled proportional counters, while the second is that of scintillators. This thesis focuses on the use of the scintillator zinc sulfide mixed with lithium fluoride for thermal neutron sensitivity.

A scintillator is a material which converts the kinetic energy of a charged particle or photon, by way of an electromagnetic interaction, into photons. For instance, as a charged particle travels through a scintillator, it gives energy to the scintillator as their charges interact. This energy can then be converted into photons by way of luminescent properties in the scintillator. This pulse of photons is very brief and, for most scintillators, is too faint for the eye to see [9].

3.2 - Zinc Sulfide

Although zinc sulfide (ZnS) was one of the first applications of a scintillator, it is still commonly used today. Its scintillations are so bright that in the early days of nuclear physics, observers used microscopes to visually observe the locations where radiation

interacted with the detection material; a property which is rare among the majority of scintillators. By the mid to late 1940s, scintillators began to be coupled to photomultiplier tubes, which made the experimentation with ZnS detectors more sensitive and qualitative [10].

When a charged particle or a gamma interacts with ZnS, a scintillation is initiated. Such a scintillation is extremely bright in comparison with other scintillators as it produces approximately 160,000 photons (^{6}Li glass, for instance, produces ~6000 photons while ^{6}LiI produces 50,000 photons) [11]. When activated with silver, ZnS scintillates at a peak frequency of 450 nm as shown in Figure 3.1. One of its interesting and important characteristics is the difference in the decay times of scintillations initiated by charged particles as opposed to gamma particles. When initiated by gammas the decay time is approximately 10ns. However, when initiated by charged particles, it is 200 ns with a bright afterglow that can extend as far as 10-100 μs. The afterglow limits the minimum separation of two pulses to 100 μs in order to provide adequate temporal resolution (this corresponds to a frequency of 10 kHz) [13]. This pulse separation is large

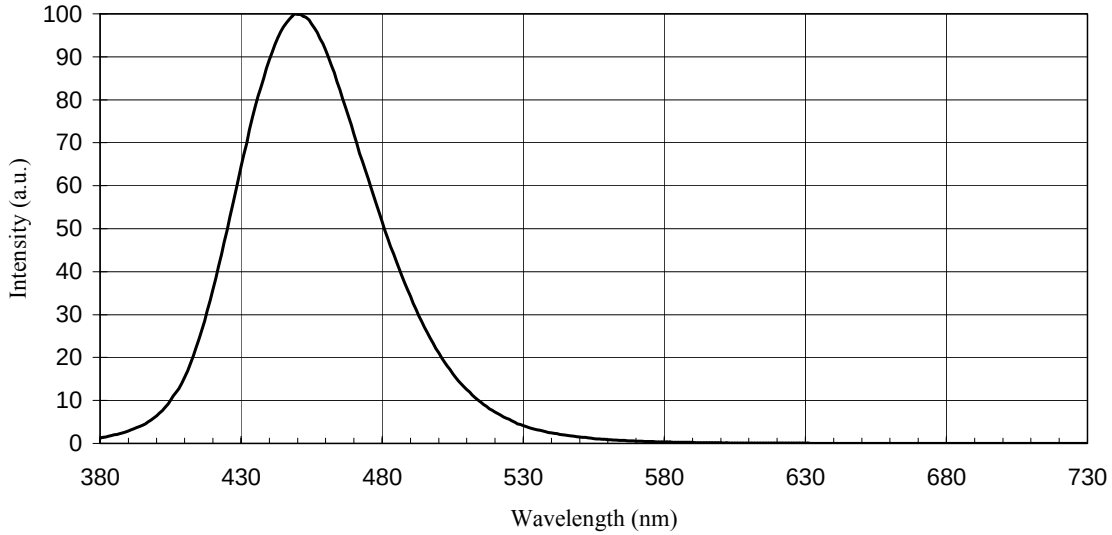

Figure 3.1 – The emission spectrum of ZnS. Courtesy of Nichia Corp [12].

in comparison with other scintillators, which severely limits the rate that scintillations in ZnS/LiF can be processed. However, such drastic differences in decay times between gamma and charged particle induced scintillations is valuable since the two can be easily separated by signal processing schemes allowing the diffraction experiments to be extremely gamma insensitive.

The detection of neutrons is complicated by their lack of an electronic charge to interact with a scintillator. This problem can easily be remedied if the scintillator can accommodate an isotope that will interact with the incident neutron by way of a nuclear reaction to produce secondary charged particles. One way of accomplishing this is by mixing into the scintillator a powdered intermediate material containing the necessary isotope to produce the charged particles. Various powdered materials have been mixed with ZnS over the years with the most popular being lithium fluoride (LiF) enriched in ^{6}Li. When neutrons interact with the ^{6}Li in the LiF, they may be captured and initiate the following nuclear reaction,

$$n + {}^{6}\mathrm{Li} \rightarrow {}^{4}\mathrm{He} + 3\mathrm{H} + 4.78\,\mathrm{MeV}$$

The alphas are emitted with an energy of 2.05MeV, while the tritons are emitted with an energy of 2.73 MeV [14]. To conserve linear momentum, both particles must be emitted collinearly in the center-of-mass frame. This capture reaction has a much larger cross section at low energies, as can be seen for the ^{6}Li(n,α)^{3}H reaction in Figure 3.2. If either or both of the alpha and triton escape the LiF and arrive at a ZnS particle, they can cause a scintillation which produces a maximum of 160,000 photons. This process is summarized in Figure 3.3.

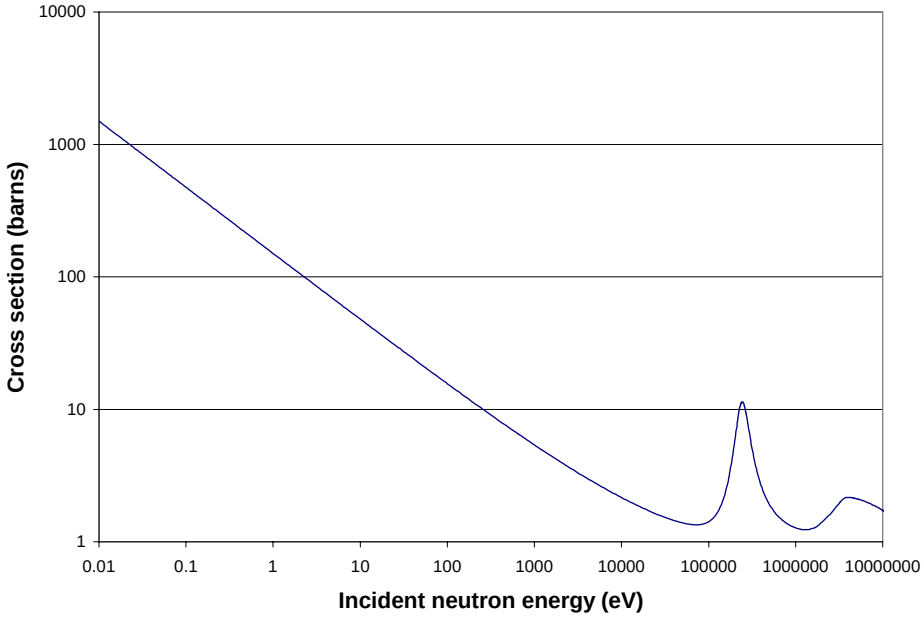

Figure 3.2 – Neutron Capture cross section for the $^{6}Li(n,\alpha)^{3}H$ reaction. Note that the cross section increases dramatically at lower energies. [15]

The size of the ZnS and LiF particles are important. The ZnS and LiF granules in commercial scintillator samples have diameters that are in the neighborhood of 5 – 10 μm. In appendix A.1 the range of the 2.05 MeV alpha is shown to be 5.9 μm in ZnS and 4.7 μm in LiF while the range of the 2.73 MeV triton is 37.8 μm in ZnS and 30.6 μm in LiF. It is then likely that a triton, with its long range, will escape the LiF granule where it was born and enter a ZnS granule to create scintillation photons. On the other hand, it is much more unlikely that the alpha will escape the LiF to create a scintillation.

The disadvantage of this scintillator is its opacity to its scintillation photons. The refractive index of LiF at 589 nm is 1.39 and for ZnS at the same frequency is 2.36 [16]. A large index mismatch exists between the two materials and their binder which leads to a rapid attenuation of light traveling through the material. For this reason, standard commercial sheets of ZnS/LiF scintillator are manufactured in thicknesses no greater than 0.5 mm [11]. This common thickness is applicable to a mixture of one part ZnS and four

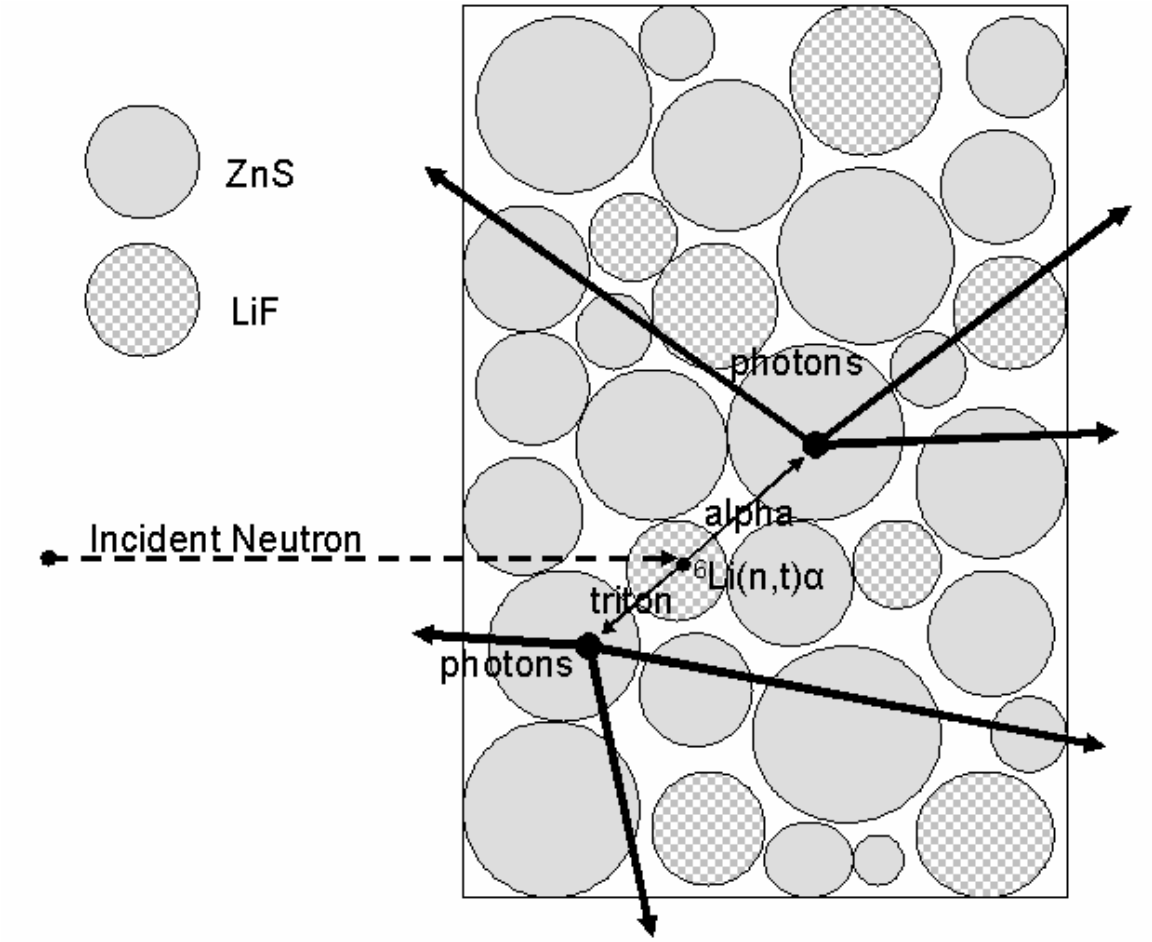

Figure 3.3 – Diagram of the Zns/LiF scintillation process with neutrons. If a neutron enters the scintillator and reacts with the ^{6}Li in the LiF, a triton and an alpha may be born. If these particles arrive at a ZnS grain, the scintillation process may be initiated resulting in 160,000 photons.

parts LiF by weight. More generally, any mixture of ZnS and LiF becomes opaque when more than 25 mg/cm^2 of ZnS are used [14].

3.3 – Wavelength-shifting Fibers

The FEFD designs examined in this thesis require the measurement of scintillation light from narrow pixel strips via a unique optical fiber known as a wavelength-shifting fiber. The design proposed for the SNS detector also uses these fibers as described in Chapter 4. Wavelength-shifting fibers are one of only a few means of creating the pixels required for these detectors.

It is outside the nature of optical fibers to trap external light which enters into their fiber core through their sides. Such light exits the opposite side at the same angle. A way around this problem is by the use of a specialized optical fiber known as a wavelength-shifting fiber, which incorporates a fluorescent material known as a fluor mixed with the plastic structure of the core. The fluor absorbs external photons that come into contact with it. Part of the energy of the absorbed photons is then reemitted with equal probability in all directions with a lower wavelength, thus the term w*avelength-shifting fiber*. A fraction of these reemitted photons will be within the critical angle of the fiber, allowing them to be trapped in and piped down the fiber length for measurement by a photon detector. All other photons escape through the surface of the fiber.

The wavelength-shifting fibers used in the SNS detector (See Chapter 4) and FEFD prototypes (See Chapter 6) are type BCF-91A wavelength-shifting fibers made by Bicron, which recently became a division of Saint Gobain Crystals and Detectors. The fiber cladding is made of the commonly used plastic polymethylmethacrylate (lucite) and the core is composed of polystyrene doped with K27 fluor [17]. The absorption and emission spectrums for this fiber are seen in Figure 3.4. Comparing this plot with Figure 3.1 shows that most of the emission spectrum from ZnS overlaps with the absorption spectrum for the fibers. Furthermore, Figure 3.4 demonstrates that there is little overlap in the absorption and emission spectra for these wavelength-shifting fibers.

An important property of the wavelength-shifting fibers is their photon trapping efficiency. This is the probability that a photon born at the location of a fluor center will travel one of the two directions possible in the fiber. For square fibers, the trapping

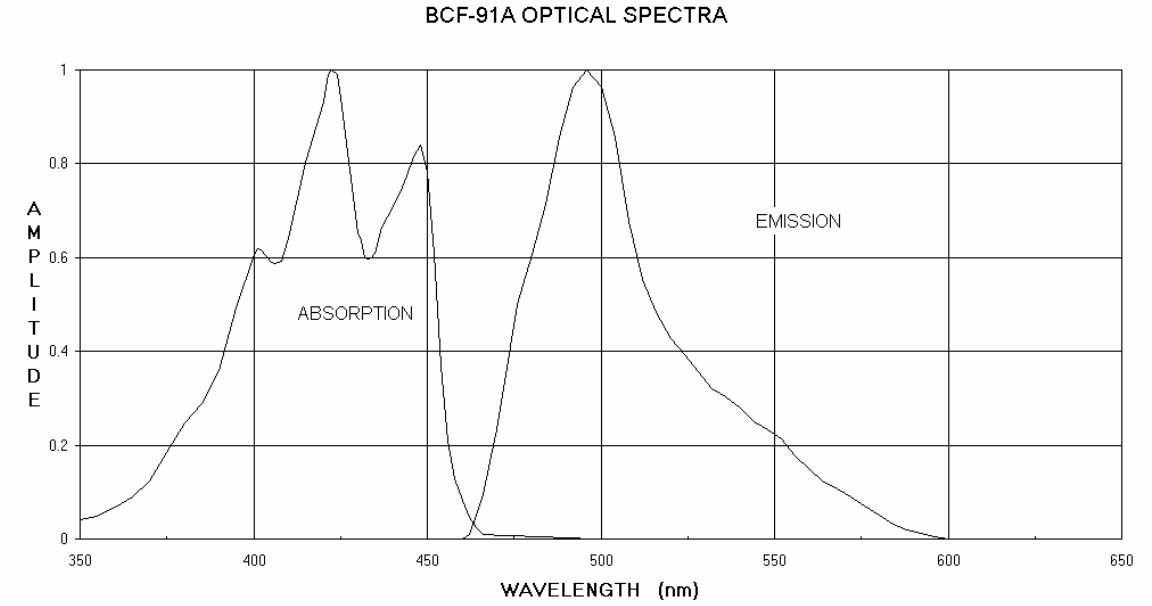

Figure 3.4 - Absorption and emission spectrum for BCF-91A wavelength shifting fibers. Courtesy of Saint Gobain Detectors and Crystals, Bicron Division [18].

efficiency is 4.4%, while for round fibers it has a minimum of 3.44%. Thus, about 25 to 30 photons must be wavelength shifted to produce one trapped photon. Since a ZnS scintillation produces up to 160,000 photons, a sufficient number should arrive at the fiber to produce a measurable quantity of trapped photons if the majority are not self-absorbed due to the opacity of the scintillator.

Wavelength-shifting fibers are not fabricated for long-length light-transfer applications, but rather for converting an external photon into a shifted-wavelength internal photon. The signal attenuates for a given length of fiber. According to the manufacturer, the 1/e attenuation length is stated as >3.5 meters for BCF-91A [19].

Chapter 4

Present Detector Designs

4.1 – The Problem with Flat-plane Detectors

Great expenditures of money will go into the development and construction of the latest generation of spallation sources (~$1.5 Billion each) by the time they are commissioned. However, the full value of these facilities cannot be realized without the installation of efficient detectors. In short, these facilities are only as effective as their detectors.

A major factor contributing to the poor performance and complexity of the present detector designs is their use as flat-plane modules necessitated by manufacturing limitations. Chapter 2 pointed out the fact that neutron diffraction from a powder sample produces Debye-Sherrer cones around an axis centered on the incident neutron beam. When a flat-plane detector module is positioned parallel to the cone axis, the Debye-Scherrer cones project themselves onto the flat detector surface as hyperbolas as shown in Figure 4.1. The complexities associated with this design approach are directly related to locating and identifying the intensity of the hyperbolae on the detector. In this case, the detector must be divided into $N \times M$ two-dimensional pixels, where N and M are the number of pixels spanning each of the dimensions. This large number of pixels significantly complicates the photon detection, signal processing, and fabrication. Ideally, one would prefer sharply defined Debye-Scherrer cones projected onto the detector as a single, straight line for the highest quality resolution and the greatest detector simplicity.

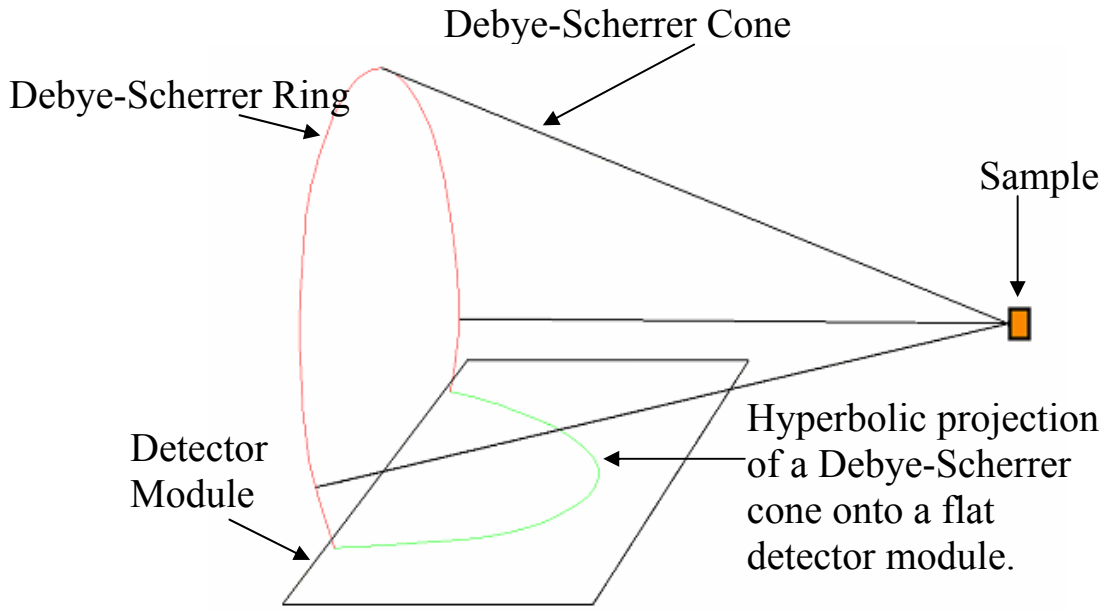

Figure 4.1 – When a Debye-Scherrer cone intersects a flat-plane detector that is parallel to its axis, a hyperbola is traced out on the surface.

This can most easily be accomplished by the straightforward approach of curving the detector into a cylindrical shape concentric with the Debye-Scherrer rings. Then the detector would only need to be divided into *N* one-dimensional pixels parallel to the Debye-Scherrer rings. This approach simplifies the detector design and reduces its fabrication costs.

Currently the most advanced detector design for powder diffraction is in use at ISIS on the High Resolution Powder Diffractometer instrument or HRPD while another design is currently under development for the SNS powder diffractometer instrument, POWGEN3. The balance of this chapter will briefly outline those designs and point out their shortcomings with will be overcome by the FEFD design discussed in Chapter 5.

4.2 – ISIS Powder Diffractometer

As mentioned in Chapter 3, the practical thickness of a ZnS/LiF scintillator sheet is limited due to opacity to about 0.5 mm. In Chapter 7 it is shown that 1 Å neutrons at normal incidence to such a scintillator sheet have a 21% probability of being captured by the ^{6}Li. However, this efficiency can be increased if the ZnS/LiF is slanted at an angle. Doing so increases the effective thickness that the neutron "sees" in passing through the sheet and the probability of being captured while keeping the physical thickness constant at 0.5 mm so that a sufficient number of photons may exit [20]. An example of the slanting of the fibers is illustrated in Figure 4.2.

The ISIS design, which is illustrated in Figure 4.3, is built upon this principle of slanted ZnS/LiF. This can be seen from the ZnS/LiF scintillator sheets which are bent in upside down "V" shaped sections. Many of the photons that pass through the scintillator surface enter the open ends of the optical fibers and are trapped as seen in the illustration.

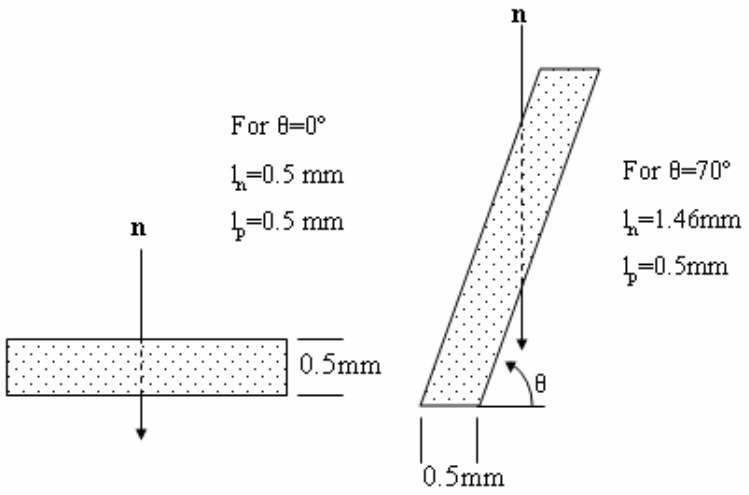

Figure 4.2 – Shown are two sheets of 0.5 mm thick ZnS/LiF scintillator which both have the same optical transmission for photons, l_n. In the sheet on the left, where neutrons are at normal incidence to the sheet, 20% of all thermal neutrons are captured. The sheet on the right is rotated by 70º which triples the path the neutrons can travel through the scintillator. This results in a 50% neutron capture efficiency.

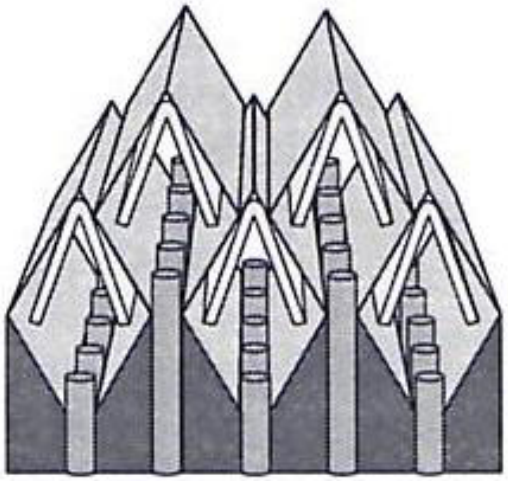

Figure 4.3 – An illustrated view of the ISIS detector. Note the upside down shaped ZnS/LiF scintillator underneath reflectors of the same shape. Under the ZNS/LiF scintillator are the ends of optical fibers which can absorb and transmit scintillation photons. Illustration from reference [21].

These fibers have a 1 mm diameter and are spaced 1 mm apart within a row and 5 mm apart between rows. To this end, the scintillator surface is divided into 5 mm by 5 mm pixels. This approach results in a high reduction in electronic noise by requiring a coincident pulse with two adjacent fibers in a row. Although, this design boasts a hefty 50% detection efficiency [21], its great drawback is its large mechanical and electronic complexity making it an expensive system to commission.

4.3 – SNS Powder Diffractometer Prototype

As the SNS facility will begin operations in 2006, it is assumed that the actual detector design will not deviate considerably from the design currently proposed. Over the past five years the in-house detector scientists at SNS have developed a detector design that, like the ISIS detector, will use ZnS as a scintillator. However, instead of collecting photons through the open ends of optical fibers it will do so through the sides of wavelength-shifting fibers.

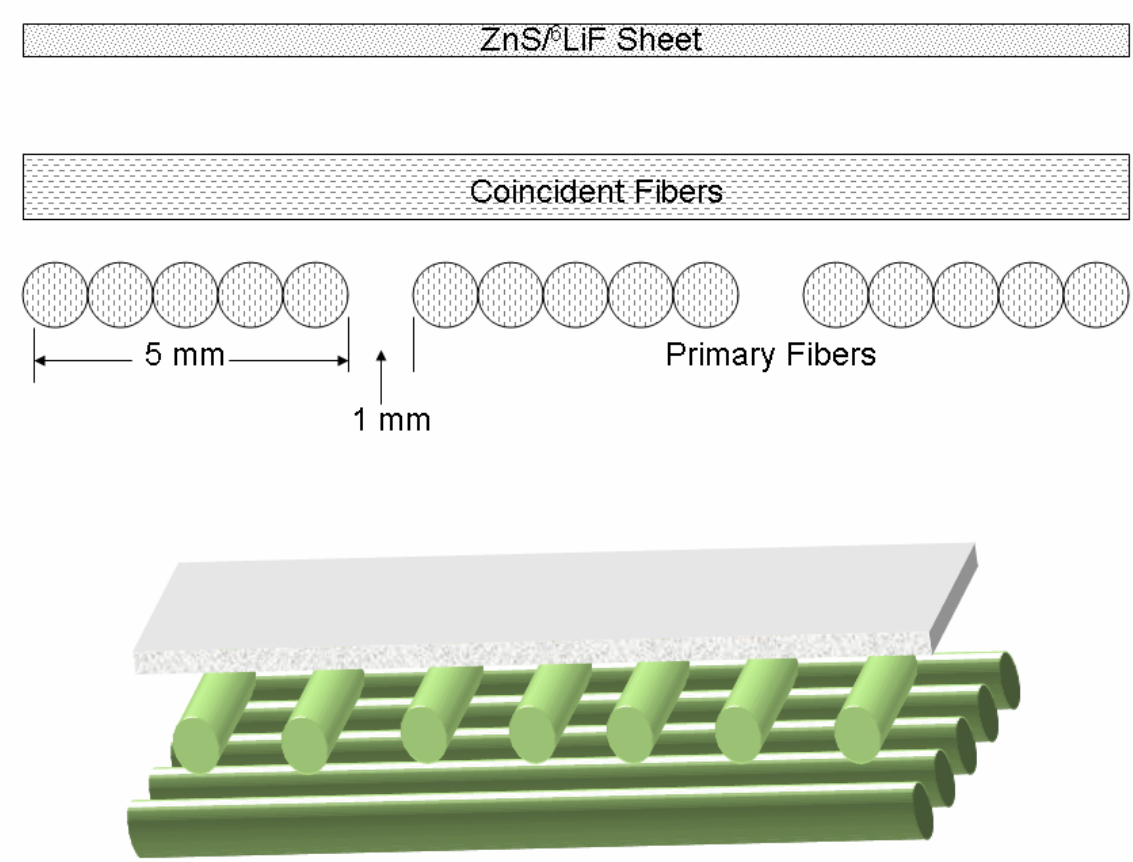

Figure 4.4 – The top illustration shows a cut-away view of the SNS detector to give the proper orientation of each detector layer. The individual pixels span 6 mm and are composed of 5 fibers to a bundle. The bottom illustration shows a three-dimensional view of this detector. Only one primary fiber bundle is included.

The SNS design, like the ISIS design, is a flat plane detector making it necessary to divide it into small, two-dimensional pixels. As previously explained, this cannot be achieved by a one-dimensional array of straight fibers but instead requires a two-dimensional array consisting of two perpendicular fiber planes. The first set, referred to as the primary fiber plane, is laid parallel to the surface of a ZnS/LiF sheet. The second set of fibers, referred to as the coincident fiber plane, is placed between the scintillator and the primary fiber plane. Figure 4.4 shows the relation of these components with an illustration of a detector unit. The coincident fiber plane is composed of 1 mm fibers with 1.5 mm spacing between fibers. This plane is placed 1.5 mm below the ZnS/LiF

screen. The primary fiber plane also contains 1 mm diameter fibers. Five consecutive primary fibers are bundled into the same photomultiplier tube, with a 1 mm gap between bundles, to define a 6 mm wide pixel. This is shown in Figure 4.4. The gap between bundles is necessary to prevent scintillation light from a single neutron capture event from entering two adjacent bundles. When a signal from the two fiber planes is shown to be in coincidence with each other, the location of a particular pixel can be tagged [22].

Two problems that the SNS design suffers from are its manufacturing complexity and its complicated fiber addressing scheme. However, a much more significant problem is the requirement of a coincident signal from the two planes of fibers. Such a requirement is hard to satisfy especially in this case where the coincident fibers shield the primary fibers from much of the scintillation light. This has the unavoidable effect of lowering the detector's performance and efficiency.

It has been shown that the ISIS design incorporates high neutron detection efficiency while the SNS design, although lower in detection efficiency, offers greater simplicity and reduced price. The FEFD design, discussed in the next chapter, combines these benefits into one detector.

Chapter 5

FEFD Design

5.1 – Basic Design

The FEFD is an exciting, new detector design for neutron powder diffraction experiments. Its development was inspired with the intent of overcoming the difficult problems discussed in the previous chapter encountered by the ISIS and SNS designs. Its characterization is central to this thesis. This detector will not only be beneficial to the facilities where it is employed but also to other users due to its high efficiency and counting rate. In addition, its design is simpler than other detector designs making it less expensive to purchase and easier to maintain. The FEFD design was initially proposed by the author and Bart Czirr of Photogenics, a Provo company devoted to neutron detection.

The detector designs discussed in the last chapter rely on fibers arranged externally to a ZnS/LiF sheet. However, the FEFD design employs gapped (i.e. spaced apart) fibers embedded throughout the interior of a ZnS/LiF scintillator sheet. This has the effect of increasing the neutron detection efficiency since 0.5mm of ZnS, the accepted maximum useful thickness, is now placed on all sides of a single fiber. A visualization of the FEFD design is shown in Figure 5.1.

Another equally significant advantage of the FEFD design is that its structure is flexible, allowing its detection surface to be bent to any curvature that the fibers can withstand. The detector can then be curved in such a way as to allow a linear strip along

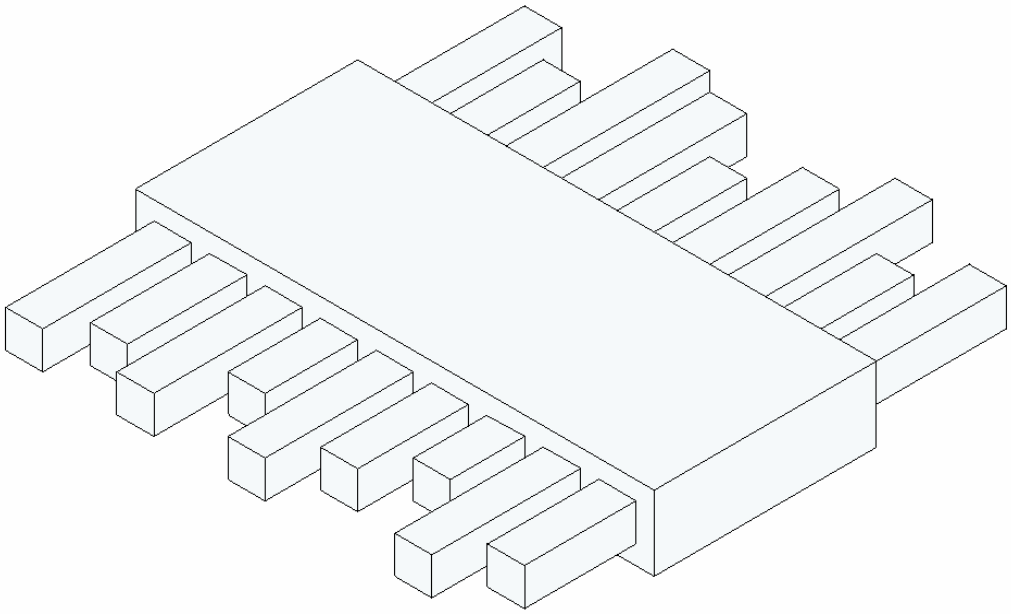

Figure 5.1 - A conceptual image of a FEFD module. This module contains square wavelength-shifting fibers embedded in ZnS/LiF scintillator.

a single wavelength-shifting fiber to intersect with a single Debye-Scherrer ring. This design then removes many of the drawbacks found in flat detectors by eliminating the need for a second set of coincidence fibers. This results in a greatly simplified detector with fewer events being discarded.

The unique ability of the FEFD design to bend and fit curves could not be achieved without the use of a nontraditional binder for the ZnS and LiF granules. This binder is known as Room Temperature Vulcanization rubber (RTV). Its initial form is a thick liquid which is mixed with the ZnS and LiF powder. Depending on the curing temperature, the RTV will cure to a solid but flexible rubber in a matter of hours or days. Using an RTV as a binder gives this detector the ability to be molded as a flat plane, then after the RTV has cured, to be bent to a cylindrical curve. The proper curvature can be maintained by permanently mounting it in a bracket.

One important consideration of the FEFD design is the gap width between wavelength-shifting fibers. As previously mentioned, 0.5 mm is the commonly accepted thickness that measurable quantities of photons can travel through a ZnS/LiF scintillator. Any scintillator further from the fibers than this distance would be ineffective. In addition, to localize the position of the Debye-Scherrer rings, scintillation photons from a captured neutron should not travel to more than one fiber. With these factors in mind, a spacing of approximately 1 mm between fibers would be needed. Further measurements would be needed to determine the optimum spacing with greater precision.

The minimum pixel width of a FEFD would be the combination of one fiber and two half-gaps. For example, if the fibers had a width of 1 mm and the gap was 1 mm, then the pixel width would be 2 mm. The ISIS and SNS detectors had pixel sizes around 5 mm wide. Similar resolution would be probably be prescribed for a FEFD and can be accomplished by bundling several consecutive fibers together to form one pixel.

5.2 – FEFD Advantages

An insightful demonstration of the FEFD's simplicity is seen in a comparison of its fiber density with the ISIS and SNS detectors. The fiber density when 1mm fibers are used in a FEFD is 500 fibers per square meter. This compares to 100,000 fibers per square meter for the ISIS detector and 1233 fibers per square meter for the SNS detector.

To summarize, the Photogenics design has the following advantages:

- The detector's surface is curved around the Debye-Scherrer rings which negates the need for coincident fibers. This increases the detector's light collection efficiency as well as simplifies signal processing.

- The overall thickness of ZnS/LiF in this design will be greater than in other designs. This has the effect of increasing the neutron capture efficiency, allowing sample runs to be shorter. This is a financial bonus to a facility and its users.
- Compared to other designs, the detector is simpler to fabricate as it will not involve a set of coincident fibers.

This list of advantages demonstrates the importance of the FEFD and contrasts its advantages over the ISIS and SNS designs.

Chapter 6

FEFD Prototype Development and Fabrication

6.1 – Scintillator Component Ratios

Four prototype modules of the FEFD design with varying fiber dimensions were constructed for testing and evaluation. However, before properly constructing these modules, the best ratio of ZnS:^{6}LiF:RTV binder had to be determined.

The common ratio of 4 parts of ZnS to 1 part of ^{6}LiF has long been used by many commercial manufactures in their ZnS/LiF scintillators. More recently, Crow, Hodges, and Cooper have shown evidence that a ratio of 2 parts ZnS to 1 part LiF may be the most ideal [22]. Additional studies are recommended to determine the most ideal ratio for FEFD modules. To keep consistency with commercially available samples, the standard ratio of 4 parts ZnS to 1 part LiF was chosen for the present analysis.

Another important ratio is that of the ZnS/LiF mixture to the RTV binder. The binder, as any material, slows down an alpha or triton with a probability of stopping them. Since this probability increases as the concentration of binder increases, it is important for this concentration to be as low as possible. However, if the amount of binder is too small, the ZnS and LiF particles are not effectively bound together resulting in poor mechanical performance and optical transmission.

To determine a ratio that satisfies the conditions just stated, literature was consulted on previously constructed ZnS/LiF scintillators. When an author constructed more than one sample, only the sample with the most dilute binder is considered. As shown in

Table 6.1, Steadman used a 3 part ZnS/LiF mix to 1 part Lucite binder mix [23]. Thomas used a mix of 3.6 parts ZnS/LiF to 1 part binder [24] while Kojima et al. used 5.5 parts ZnS/LiF to 1 part binder [25]. Using ratios in Table 6.1 as a guide, it was decided that a ratio of 4 parts ZnS/LiF to 1 part RTV binder would provide the necessary structural strength while being dilute enough to minimally impede the alpha and triton particles. To this end, the complete ratio for the components in the scintillator for the FEFD prototypes was chosen to be 4 parts ZnS, 1 part LiF, and 1.25 parts RTV binder.

Author	$\frac{\text{Parts ZnS/LiF by wt.}}{\text{1 Part Binder by wt.}}$	Percent binder by weight
Steadman	3	25.0%
Thomas	3.6	21.7%
Kojima et al.	5.5	15.4%
FEFD Prototypes	4	20.0%

Table 6.1 – Comparison of the weight ratio of ZnS/LiF to binder used by others as well as for the FEFD prototypes constructed for this thesis.

Both the ZnS and LiF were purchased from Eljen Technology. According to the manufacturer, the distribution of the ZnS particles is guaranteed to be between 8 – 10 μm. No claims were made for the size distributions of the LiF particles, however, they were described as "finely ground" with a 95% ^{6}Li enrichment. The ZnS and LiF are from the same quality and size distribution that Eljen uses to manufacture their commercial ZnS/LiF thermal neutron detectors [26].

6.2 – FEFD Prototype Fabrication

The fabrication of the FEFD modules was aided by molds made by Wesley Liffreth of the BYU Physics Department machine shop. One two-part mold set was used to fabricate both of the 1 mm fiber prototypes while another set was used to fabricate both

of the 2 mm fiber prototypes. A set of molds with the dimensions for the 2 mm fibers is shown in Figure 6.1. The molds in a set were used in a particular order during fabrication and will be designated as mold #1 and mold #2. This designation will be important in the following description of the mold fabrication.

The SNS POWGEN3 instrument is designed with 6 mm wide pixels [22]. The FEFD prototypes were designed to have approximately the same pixel width when several fibers are bundled together. Although the molds are capable of fabricating prototypes with up to seven fibers for the 1 mm fiber prototype and up to five fibers for the 2 mm fiber prototype, each prototype was characterized with only one pixel consisting of three fibers since this is all that is needed to determine the neutron capture efficiency. This gave a pixel width of 6 mm for the two 1 mm fiber prototypes and a pixel width of 9 mm for the 2 mm fiber prototypes. To produce a single pixel during the experiments (Chapter 8), all three fibers in a prototype were bunched together and routed to the same photomultiplier tube.

The fabrication of the prototypes follows from the illustrations in Figure 6.1. After the wavelength-shifting fibers have a coat of GE Silicones SS4120 primer applied to their surface, which aids in the adhesion of the binder to the fibers [27], they are fastened into the channels of mold #1 with small dabs of water soluble glue as shown in the top illustration of the figure. When the glue has hardened, the ZnS/LiF/RTV scintillator compound, which has a thick, pasty consistency, is packed into the mold. The mold is then placed in a bell jar under vacuum to remove the significant quantities of trapped air in the uncured scintillator. A flat plate is then clamped onto the mold over the uncured scintillator to give a smooth and level surface to the scintillator compound.

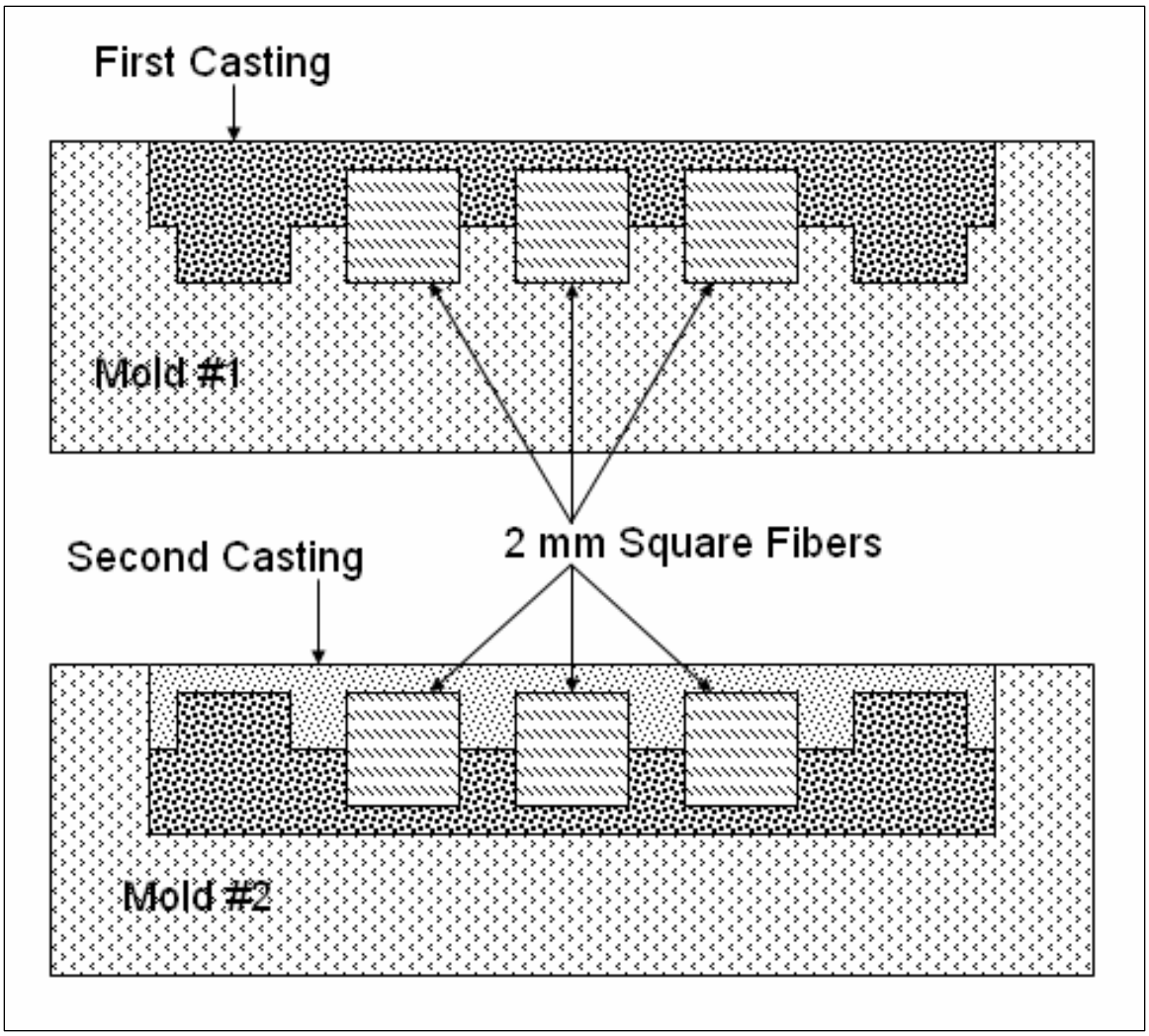

Figure 6.1 – End view of the set of molds for fabricating the 2 mm FEFD prototypes. Fibers are first placed into the channels of the mold #1 and the scintillator is packed around it. After the scintillator has cured, the partially completed prototype is removed from mold #1 and placed into mold #2 were additional scintillator is applied and cured. When this curing is complete, the finished prototype is removed from mold #2. Not shown are the plates which are clamped over the scintillator in both molds to form a flat surface. Also note that fibers were placed in only three of the five available channels.

The rate at which an RTV cures is dependent upon the curing temperature. GE Silicones claims that RTV615, the RTV used for the prototypes, fully cures in 6-7 days at 25ºC but is accelerated to 4 hours at 65ºC [28]. After the evacuation process the molds were cured at 50ºC since this was a temperature which would allow curing in hours while being cool enough not to affect the plastic fibers.

After curing, this partially finished stage of the prototype is removed from the mold#1, turned upside down and placed into mold #2 as shown in Figure 6.1. Before hand, a fresh coat of GE Silicones SS4120 primer must be applied to the fiber surfaces before placement into the mold. In this mold additional ZnS/LiF/RTV scintillator compound was packed in to cover the exposed fiber surfaces. As with mold #1, the scintillator compound is degassed in an evacuated bell jar and then a flat plate is clamped to the exposed surface of the mold. It is cured at 50ºC.

After this curing, the prototype was removed from the mold as a completed unit. The fiber ends were then cut to equal lengths and polished to a smooth finish. A picture of the four prototype modules is shown in Figure 6.2.

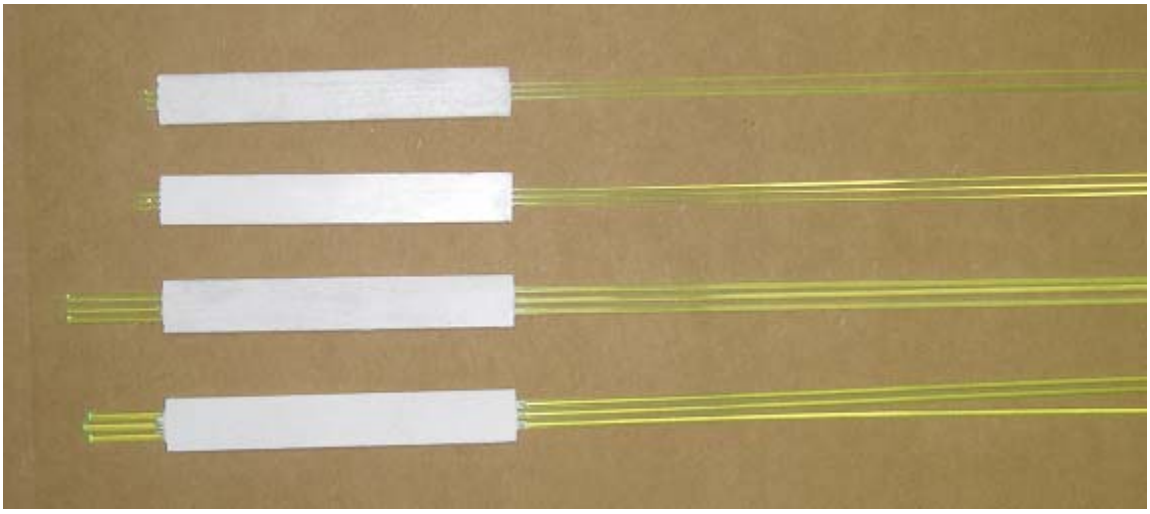

Figure 6.2 – The fabricated FEFD detectors. The fiber sizes and dimensions from top to bottom are 1 mm square, 1 mm round, 2 mm square, 2 mm round. The fibers exiting the right side of the photo were coupled to a photomultiplier tube.

Chapter 7

FEFD Efficiency Calculations

7.1 – Utility of MCNP

When ^{6}Li captures a neutron, an alpha and a triton are born. Since the number of scintillations is dependent and proportional to the number of neutron captures, an important parameter for a neutron detecting scintillation detector is its neutron capture efficiency. Computational methods for investigating the neutron capture efficiency of a scintillator are a powerful element for optimizing the physical parameters in the detector design. Before the FEFD prototypes were fabricated, computations were made to approximate their expected performance and to compare them with the ISIS and SNS detector designs.

Nuclear processes, being random in nature, are not easily modeled by deterministic equations. However, statistical sampling applies particularly well to this situation. A well accepted and effective computational method which relies on statistical sampling is known as the Monte Carlo method. This method can be applied for calculating the overall outcome of many random nuclear interaction probabilities with materials. Monte Carlo calculations are precise to within an error determined by the number of interactions included in the calculation. Such methods have only come into common use since the inception of modern computing devices with the first practical application being for the design of nuclear weapons during World War II.

A Monte Carlo computer code that is very versatile for calculating the outcome of collisions from neutrons, photons, or electrons in different materials is the Monte Carlo N-Particle transport code or simply MCNP which was developed at Los Alamos National Laboratory. The latest version, MCNP5, was utilized to computationally determine the neutron capture efficiency of the FEFD prototypes before they were fabricated [30].

The convenient power of MCNP, as can be said with many other trusted computational techniques, is that it can nowadays be used to determine results for a model on a desktop computer. This power has the advantage, as long as the user is aware of its limitations, of providing direction for the improved development of the model.

7.2 – MCNP Calculations

Individual MCNP programs files were run to calculate the ^{6}Li neutron capture efficiencies of each of the four modeled FEFD prototypes at several different neutron beam energies. After each computation, an output file was produced containing the results from which the neutron capture efficiency could be calculated. The input energies were calculated over a much larger range than the 0.005 to 0.1 eV thermal energy range to gain a more general feel for the manner in which neutrons interact with the detectors. Calculations were made with energy points at 0.001, 0.0025, 0.005, 0.01, 0.0253, 0.081803, 0.2, 0.5, 1.0, 2.5, 5.0, 10.0, 25, 50 and 100 eV and are tabulated with their associated neutron capture efficiency in Table 7.1. Most of these energy points were chosen to produce a smooth curve on a semi-log chart as shown in Figure 7.1; however, 0.0253 eV and 0.081803 eV were chosen as they correspond to thermal equilibrium and

	EFFICIENCY BY CONFIGURATION				
Energy (eV)	1 mm round	1 mm square	2 mm round	2 mm square	0.5 mm Flat Sheet
0.001	0.981	0.977	0.980	0.972	0.870
0.0025	0.965	0.956	0.967	0.948	0.735
0.005	0.933	0.916	0.944	0.912	0.614
0.01	0.873	0.852	0.901	0.857	0.492
0.0253	0.749	0.722	0.804	0.747	0.349
0.081803	0.544	0.519	0.616	0.556	0.212
0.2	0.401	0.381	0.472	0.422	0.141
0.5	0.280	0.265	0.341	0.302	0.0920
1.0	0.210	0.199	0.261	0.231	0.0661
2.5	0.141	0.133	0.179	0.158	0.0424
5.0	0.105	0.0996	0.137	0.121	0.0307
10.0	0.0771	0.0729	0.102	0.0895	0.0219
25.0	0.0507	0.0478	0.0680	0.0598	0.0139
50.0	0.0366	0.0345	0.0498	0.0438	0.00991
100	0.0264	0.0249	0.0364	0.0320	0.00707

Table 7.1 – MCNP calculations for each of the FEFD designs and 0.5 mm thick sheet at various energy settings.

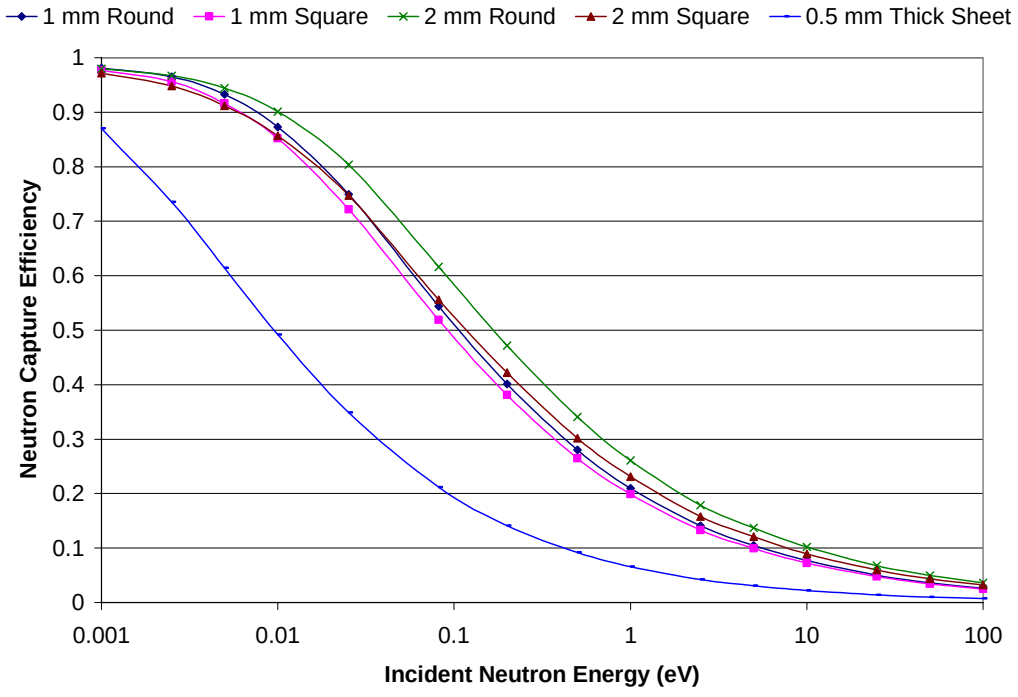

Figure 7.1 – Plot of the tabulated MCNP calculations shown in Table 7.1 for each of the four FEFD configurations and the 0.5 mm thick sheet.

1 Å neutrons respectively, which are both important benchmarks. It should be noted that these calculations were made with the assumption of no optical attenuation.

Although each of the detectors considered in Figure 7.1 show neutron capture efficiencies that closely parallel one another, some important results can be gleaned. First at low energies, the neutron capture efficiencies appear very high and seem to converge for all detectors. This convergence effect can be explained by noting that the efficiency of the 0.5 mm flat sheet detector is also converging towards 1 in this limit. When neutrons enter a FEFD they first encounter a similar 0.5 mm scintillator region bounding the surface where, for very low energies, they have the same high probability of being captured. In addition, these detectors contain additional scintillator which causes the total neutron capture efficiency to be close to 100% for all four FEFD detectors. This high capture probability at low energies is due to the fact that the ^{6}Li capture cross section increases with decreasing neutron energy proportionally to the inverse of the neutron's velocity as is seen in from Figure 3.2 for the $^{6}Li(n,\alpha)^{3}H$ reaction [14]. Thus, the lower a neutron's energy or the longer its wavelength, the more likely it is to be captured.

Figure 7.1 gives the impression that the neutron capture efficiencies of the different FEFD's converge at high energies, however, such an assumption is faulty. Figure 7.2 shows a plot of the data points from Table 7.1 which have been normalized to the 2 mm round fiber detector. In this figure it is seen that no such convergence occurs. Furthermore, the neutron capture efficiencies of similarly shaped fibers of different sizes largely parallels each other.

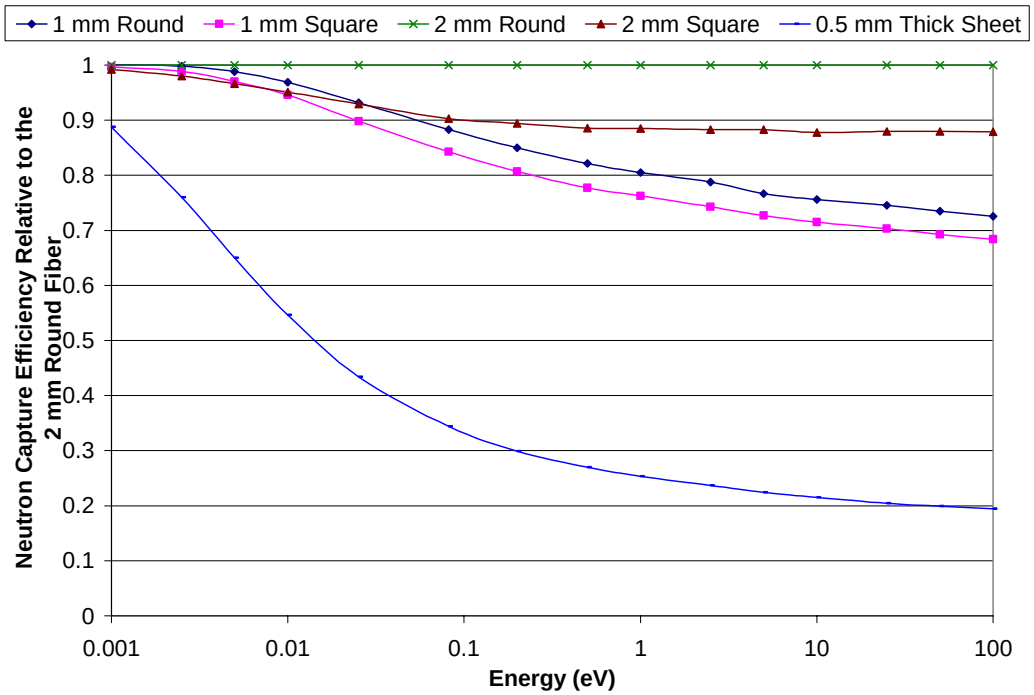

Figure 7.2 - Plot of the tabulated MCNP calculations shown in Table 7.1 normalized to the 2 mm round fiber detector.

Perhaps the most important observation is that the 1 and 2 mm round fibers have a higher neutron capture efficiency than the 1 and 2 mm square fibers, respectfully, which becomes more pronounced at higher energies. As the incident neutron energies increase, neutrons are more likely to penetrate past the 0.5 mm thick scintillator region above the fiber plane and into the scintillator between the fibers. Since a square fiber occupies 21.5% more volume that a round fiber of the same width and length, the detector with round fibers contains this much more scintillator allowing it to capture more neutrons. It has thus been seen that both the fiber shape and size have an important bearing on a detector's efficiency.

Chapter 8

Efficiency Measurements

8.1 – Measurement Theory

The intrinsic neutron counting efficiency, ε, of a detector may be given in general terms by,

$$\varepsilon = \frac{N}{R} \tag{8.1}$$

where N is detected neutron flux and R is the incident neutron flux entering the detector [14]. If Φ is the neutron fluence crossing a flat detector surface at normal incidence and A is the area of the surface, $R = \Phi A$. Then for a uniform field of neutrons at normal incidence to a flat detector surface, Equation 1 may be expressed as,

$$\varepsilon = \frac{N}{\Phi A} \tag{8.2}$$

An experimental setup was constructed to measure the neutron counting efficiency of the four FEFD prototypes. It was necessary to use a flux monitor for determining the fluence at the detector. Using subscripts of d and m for the detector and flux monitor respectively, the relation for the flux at the detector when the flux at the flux monitor is known is given by,

$$\Phi_d = \frac{r_m^2}{r_d^2}\Phi_m \tag{8.3}$$

where r_d and r_m are the distances from the source to the detector and flux monitor respectively. In addition, Equation 8.2 may be tailored to the detector and flux monitor as,

$$\varepsilon_d = \frac{N_d}{\Phi_d A_d} \qquad (8.4) \qquad\qquad \varepsilon_m = \frac{N_m}{\Phi_m A_m} \qquad (8.5)$$

Equations 8.3-5 may be combined to give the detector efficiency as,

$$\varepsilon_d = \frac{N_d}{N_m} \cdot \frac{r_d^2}{r_m^2} \cdot \frac{A_m}{A_d} \cdot \varepsilon_m \qquad (8.6)$$

The following experimental setup and measurements will take advantage of this equation to determine the efficiency of the detectors.

8.2 – Experimental Setup

Unlike the MCNP calculations, which were performed in a convenient office location, the prototypes had to be tested at a facility that could provide a neutron beam with time-of-flight characteristics such as a spallation source. Time-of-flight neutrons provide the benefit selecting a specified energy range which was necessary for these measurements. Only a few spallation source facilities exist worldwide with two residing in the United States; those are IPNS at Argonne National Laboratory in Illinois and LANSCE at Los Alamos National Laboratory in New Mexico. Arrangements were made with Dr. Kenneth Littrel at IPNS to use their CHEX instrument.

CHEX consists of a cavity for experimental purposes measuring roughly one meter wide, two meters long and 3/4 of a meter tall. In the center of the cavity is a cylindrical aluminum canister aligned with its axis in the vertical direction having a 30.5 cm inside diameter and a 32.4 cm outside diameter. The incident and exit beamlines are welded to

openings at opposite ends of the canister with the exit beamline terminated into an absorber. Defining θ=0º in the direction of the neutron beam, this canister has 4 thin measurement windows at θ=45º, 135º, 225º and 315º as shown in Figure 8.1.

For these experiments, CHEX was configured with a cylindrical vanadium target in the center of the canister. This target had a 0.635 cm diameter and a length of 7.6 cm and had its axis aligned with the canister's. Due to its high inelastic scattering cross section and low elastic scattering cross section, the vanadium target was expected to scatter neutrons isotropically without changing their energy [30]. The FEFD's were placed outside the window at θ=135º with the fibers running perpendicular to the axis of the canister. The measurement cavity in CHEX is not light-tight which made it necessary to provide a light-tight enclosure for the detector. Due to its versatility, two inch diameter ABS pipe was used to encase both the detector and the transparent portion of the photomultiplier tube. The window at θ=45º was used for a flux detector. An aluminum cylinder that was closed at one end was used for its light-tight enclosure. This configuration is illustrated in Figure 8.1.

One end of each of the three fibers in a FEFD detector was coupled to a 2 inch Burle S83019F photomultiplier tube with the aid of a lucite fiber holder. This fiber holder consisted of three channels drilled through the lucite to align the fibers with the front face of the photomultiplier tube. The signal produced in the photomultiplier tube with photons from the fibers is carried from the tube's anode to an Ortec 2020 spectroscopy amplifier. After amplification, the signal is terminated into a multichannel analyzer where the spectrum was recorded. The integrated sum of this spectrum gives the total number of neutrons counted or N_d in equation 7. The multichannal analyzer

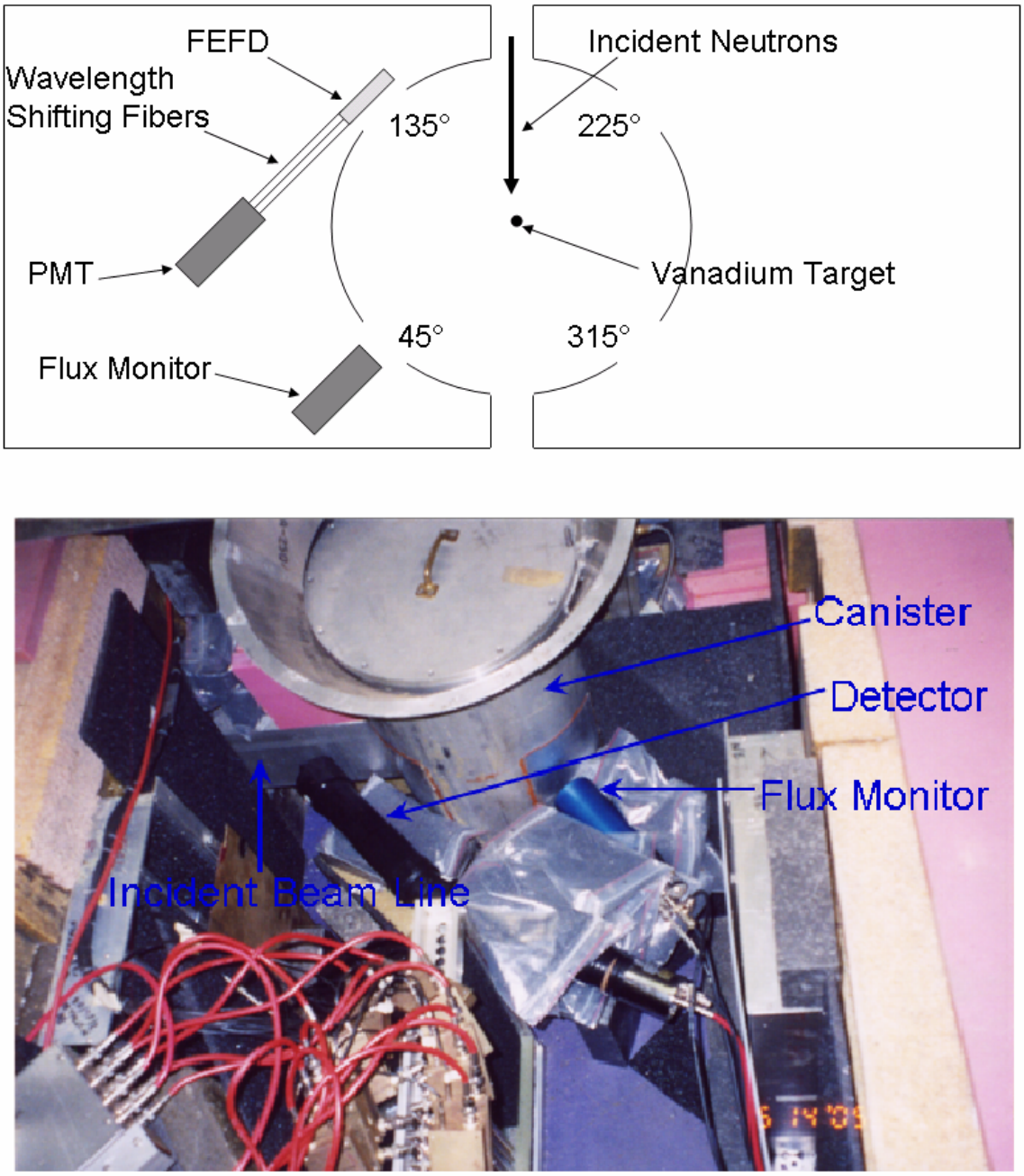

Figure 8.1 – Detector setup in the CHEX instrument. The illustration at the top of the figure shows a diagram of the individual components in the cavity of the CHEX instrument. The picture at the bottom of the figure shows the actual setup. Note that the detector was encased in ABS tubing to allow a light-tight structure. The red wires and additional equipment shown are part of the standard CHEX instrument used for purposes outside the scope of these measurements.

was gated to only accept events that coincided with 1Å neutrons centered on a 0.5 ms wide time window.

The flux monitor consisted of a 3.160 cm × 3.405 cm (10.760 cm^2) pane of 0.211 cm thick GS-20 ^{6}Li scintillating glass which was manufactured by Applied Scintillation Technologies to be 95% enriched in ^{6}Li. It was shown by chemical analysis to have a Li content of 5.597% [31]. From these parameters, an MCNP calculation gave a neutron capture efficiency of 0.7741 for a 1Å neutron beam at normal incidence to the pane. A value of $\varepsilon_m = 0.7741$ will be used in the analysis that follows.

The GS-20 glass was optically coupled to a Burle S83019F photomultiplier tube with the tube's dynode signal terminated into an Ortec 584 constant fraction discriminator NIM module. This unit is designed to discard pulses and noise below a set amplitude level. For this case, the discriminator setting was placed in a valley below the ^{6}Li neutron capture peak from the GS-20 glass but above the noise which becomes significant at low signal amplitudes. The much cleaned-up signal from the discriminator unit was sent to an Ortec 872 quad counter/timer for counting. The flux monitor counter was gated with the same time window as the detector. The instrument setup is depicted in Figure 8.2.

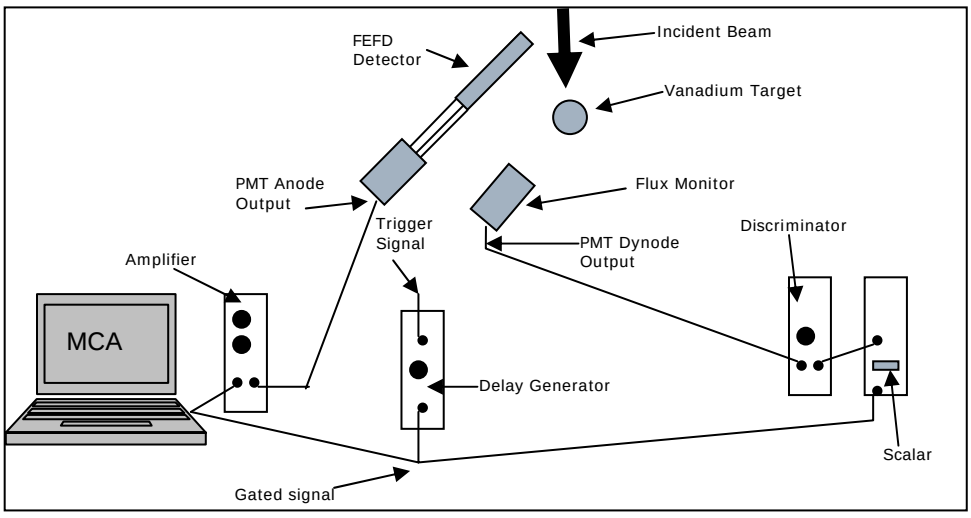

Figure 8.2 – Instrumentation depiction for the detector and flux monitor.

8.3 – Flux Monitor Calibration

The values of N_m, A_m, r_m, ε_m must be determined for the flux monitor to use equation 8.6. Since ε_m has already been determined and A_m and r_m may be readily found from trivial measurements, N_m is the remaining value to be determined. When the spectrum produced from a GS-20 glass scintillator is examined, a ^{6}Li neutron capture peak superimposed on a background spectrum is seen. It is important to isolate the true ^{6}Li neutron capture events from the background. For these measurements, a calibration run was made to determine the ratio of flux monitor counts on the Ortec 872 quad counter/timer that were true ^{6}Li neutron capture verses total counts.

The calibration run was made for the GS-20 glass using the same configuration for the counter as will be used with the detector measurements. However, the anode of the flux monitor's photomultiplier tube was connected to an Ortec 2020 spectroscopy amplifier. After amplification the signal was terminated into a multichannel analyzer with the same gating as the counter. Figure 8.3 shows the spectrum obtained with the multichannel analyzer for the calibration run. The ^{6}Li neutron capture peak was considered to extend from channel 250 to channel 450 and was found to contain 8.953×10^5 events. In this region, the gamma/noise background under the peak fits a sloped line fairly well under which were found 0.317×10^5 background events. After this background is subtracted from the peak, there are a total of 8.636×10^5 ^{6}Li neutron capture events compared with 1.088×10^6 events on the counter which gives a ratio of 0.794. This implies that 79.4% of the events on the counter are due to ^{6}Li neutron

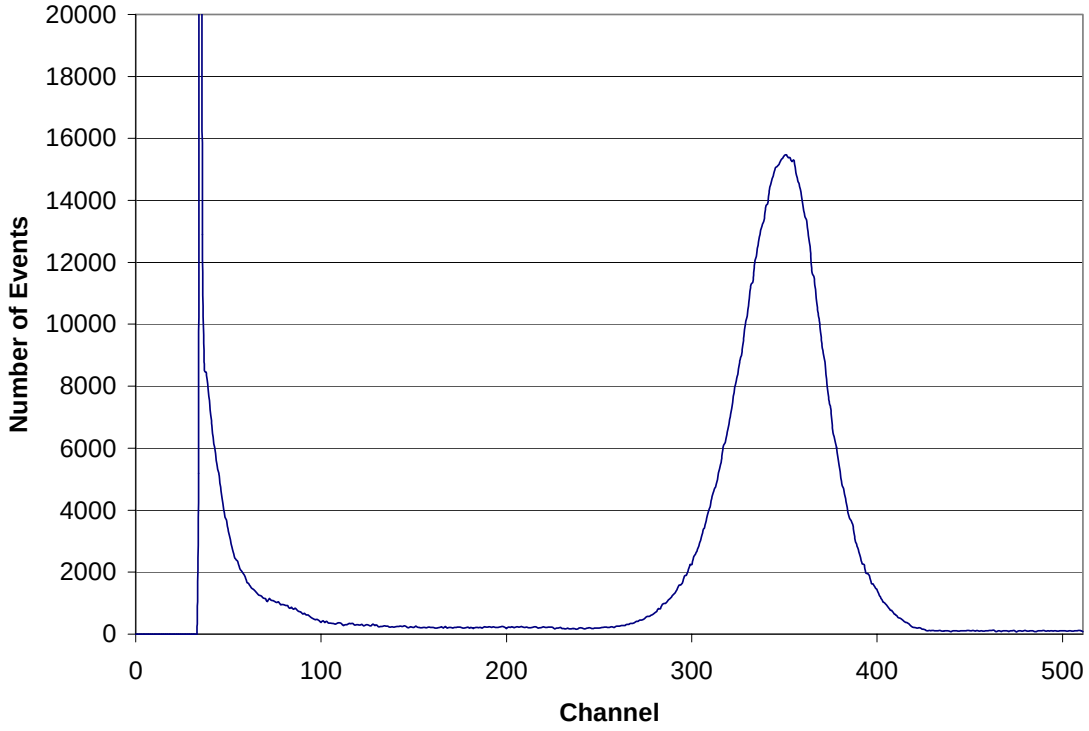

Figure 8.3 – Spectrum of the flux monitor calibration run. The peak at channel 350 is due to ^{6}Li neutron capture and is superimposed on a background.

capture. If K_m is the number of counts given by the Ortec 872 quad counter/timer,

$N_m = 0.794 \cdot K_m$.

8.4 - Results

The detector measurements took place on May 11-14, 2005. As mentioned in Section 8.2, the same gate signal was used for both the detectors and flux monitor which was centered on 1Å neutrons and had a width of 0.5 ms. For each of the four FEFDs, individual data runs were made for gain settings of 70, 90 and 150 on the Ortec 2020 spectroscopy amplifier. The total number of counts each detector produced, N_d, during a measurement run is the sum of all multichannel analyzer spectrum events and are listed in Table 8.1 for each detector and gain setting. In a similar manner, for each

measurement run the total number of counts from the flux monitor, K_m, was displayed on the Ortec 872 quad counter/timer and is given in Table 8.2 for each detector and gain setting.

Gain Setting	1 mm Square	1 mm Round	2 mm Square	2 mm Round
150	86,189	166,195	60,072	125,314
90	105,074	113,441	101,715	98,893
70	249,639	81,513	124,152	106,923

Table 8.1 – Total number of FEFD events counted for each displayed detector and gain setting. Each entry is a value for N_d in equation 8.6.

Gain Setting	1 mm Square	1 mm Round	2 mm Square	2 mm Round
150	185,660	345,656	74,566	104,898
90	310,733	311,016	178,107	152,408
70	930,386	266,171	255,675	197,569

Table 8.2 – Total number of flux monitor events counted for each displayed detector and gain setting. Each entry is a value for K_m in equation 8.6.

The spatial parameters for each of the detectors and the flux monitor are listed in Table 8.3.

Detector Parameters	Flux Monitor	1 mm Square	1 mm Round	2 mm Square	2 mm Round
Surface Length (cm)	3.405	10.0	10.0	10.0	10.0
Surface Width (cm)	3.160	0.6	0.6	0.9	0.9
A_d (cm^2)		6.0	6.0	9.0	9.0
A_m (cm^2)	10.76				
r_d (cm)		25.14	26.14	25.14	24.89
r_m (cm)	19.77				

Table 8.3 – Important spatial parameters for each detector and the flux monitor. The areas were calculated by multiplying the length by the width and the solid angles were found by the use of equation 8.8.

With the information for the detectors and the flux monitor given in Tables 8.1-3 coupled with the calculated neutron capture efficiency of 0.7741for flux monitor, as was shown in Section 8.2, Equation 8.6 may be used to find the neutron detection efficiency of each detector at the specified gain setting. It should again be noted that $N_m = 0.794 \cdot K_m$. These results are shown in Table 8.4.

Gain Setting	1 mm Square	1 mm Round	2 mm Square	2 mm Round
150	1.312	1.470	1.518	2.207
90	0.956	1.115	1.076	1.199
70	0.759	0.936	0.915	1.000

Table 8.4 – Measured efficiencies for each FEFD detector and gain settings for 1 Å neutrons.

The surprising outcome observed from Table 8.4 is that many of the measured efficiencies are unrealistically higher than the physical limit of 1.0. In addition, these efficiencies are approximately 2 – 4 times larger than was predicted by MCNP as shown in Table 7.1. Such results may be due to two reasons:

- The neutron scattering from the vanadium target was not isotropic as initially thought. The detectors may be receiving a higher flux of neutrons than the flux monitor as they are angled more towards the face of the vanadium being struck by the incident neutrons.
- There may be a significant component of background flux that must be subtracted from the total neutron flux.

These unsatisfactory solutions are the first step in a process of determining the true neutron detection efficiencies of the FEFD prototypes. CHEX has been reserved for the month of August 2005 to investigate the factors that have led to these results. At that time accurate data will be obtained for the publication of a paper in the near future.

An interesting feature that is observed in Table 8.4 is the increase in efficiency with an increase in gain for an individual detector. This is inline with expectations based on the shape of the pulse-height spectrum obtained from the FEFD detectors. The majority of the counted events are contained in the low pulse-height channels with a rapidly decaying tail in the high pulse-height channels. As the gain is increased, a larger number of counted events is included in the spectrum since more amplified events are brought into the low pulse-height channels.

Although the measured intrinsic efficiencies of the FEFD detectors are well above expectations, the relative efficiencies of the FEFD detectors compared reasonable well with the relative MCNP efficiencies. It must be noted that MCNP can only be used as a rough guide since it can only calculate the ^{6}Li capture efficiency and not optical attenuation in the scintillator. Table 8.5 lists the relative efficiencies for the FEFDs with respect to the efficiencies of the 2 mm square fiber prototype normalized to 1.000. It is unclear why the relative efficiency of the 2 mm round fiber detector with a gain of 150 is inconsistent with the other gain settings and, perhaps, this measurement should be ignored. Otherwise, there is relatively good agreement between the measured relative efficiencies for each detector between gain settings.

Gain Setting	1 mm Round	1 mm Square	2 mm Round	2 mm Square
150	0.968	0.864	1.454	1.000
90	1.036	0.888	1.114	1.000
70	1.023	0.829	1.092	1.000

Table 8.5 – Measured efficiencies for the FEFDs relative to the 2 mm round prototype across gain settings.

Table 8.6 lists the calculated MCMP efficiencies relative to the 2 mm square fiber prototype. These calculated efficiencies were made with the assumption that the scintillator is transparent so that photons from each ^{6}Li neutron capture in the scintillator are detected.

1 mm Round	1 mm Square	2 mm Round	2 mm Square
0.978	0.933	1.108	1.000

Table 8.6 – Calculated Efficiencies relative to the 2 mm round prototype with no photon attenuation.

By comparing the two tables, it can be seen that for the 2 mm square and round fiber detectors, the FEFD relative measured efficiencies compared fairly well with the relative MCNP efficiencies. However, for the 1 mm round and square fiber detectors, contrasting results were obtained. The 1 mm square fiber detector produced relative measured efficiencies that were approximately 7 - 10% lower than the calculated MCNP results. On the other hand, the 1 mm round fiber detector produced a relative measured efficiency for the gain setting of 150 that matched the MCNP results while the relative measured efficiencies of the other two gain settings disagreed with the MCNP results by 4 – 6%. It may be of interest to consider the situation where photons are not allowed to travel over 0.5 mm in the scintillator as advertised in the literature. Configuring MCNP with this assumption gives the results for the calculated efficiencies relative to the 2 mm round fiber detector listed in Table 8.7. These results deviate further from the measured results in Table 8.5 than do the calculations with no attenuation in Table 8.6, and suggest that the

1 mm Round	1 mm Square	2 mm Round	2 mm Square
0.745	0.907	0.783	1.000

Table 8.7 - Calculated Efficiencies relative to the 2 mm round prototype with 0.5mm photon attenuation within.

optical attenuation length is greater than 0.5 mm in ZnS/LiF scintillator. This optical attenuation length will be carefully examined for the mixtures of interest in future work.

In summery, the relative efficiencies of FEFDs may be approximated by the use of MCNP calculations. Although the absolute efficiencies were not obtained in the measurements, evidence from the absolute MCNP calculations and the close match of the measured relative efficiencies with the MCNP relative efficiencies points to the absolute efficiency of the FEFDs tested of being around 50%.

Chapter 9

Conclusion and Recommendations

Being motivated by the encouragingly high MCNP ^{6}Li neutron capture efficiency calculations, great efforts must be placed on the further on further development of the FEFD detectors. This thesis lays the groundwork for further efforts in this direction. With these efforts, it is envisioned that the FEFD design will replace present detector designs.

The FEFD will be a detector design that neutron scattering facilities cannot overlook for their neutron scattering instruments. The FEFD will offer three important advantages. Listed in order of their importance they are

- Design simplicity - the FEFD design simplicity will allow for greater solid angle coverage of the sample and lower maintenance downtime.
- Low price - the issue of price is of utmost importance due to the tight budget constraints for detectors and instrumentation.
- High neutron detection efficiency – the high neutron detection efficiency will allow more users to cycle through a facility, increasing its scientific productivity. In addition, this high efficiency will allow for shorter experiment times and smaller samples.

Further development is required for the practical operation of the FEFD design. It is recommended that:

- A wider range of fiber sizes be investigated for use in the detectors.

- The optimum gap width between fibers be studied.
- Computational modeling of photon transfer through the Zns/LiF scintillator be attempted to better optimize the final design.
- Different ratios of ZnS to LiF be investigated for a more optimized scintillator.
- Requiring coincidence pulses from both ends of the optical fibers to reduce noise be studied.

Using these recommendations and the lessons learned in this thesis, the FEFD has the potential of becoming a best-in-class design for powder diffraction instruments.

BIBLIOGRAPHY

[1] R. Jenkins, R.L. Snyder, *Introduction to X-ray Powder diffractometery* (Wiley, New York, 1996).

[2] G.L. Squires, *Introduction to the Theory of Thermal Neutron Scattering* (Cambridge University Press, Cambridge, 1978).

[3] R Pynn, Neutron Scattering – A Primer, in *Los Alamos Science*, **19**, 1 (1990).

[4] R. K. Crawford, *Advances in Neutron Scattering Instrumentation*, Edited by I.S. Anderson and B. Guerard, Proceedings SPIE 4785 (SPIE, Bellingham, Washington, 2002).

[5] M. Furusaka, *Advances in Neutron Scattering Instrumentation*, Edited by I.S. Anderson and B. Guerard, Proceedings SPIE 4785 (SPIE, Bellingham, Washington, 2002).

[6] B. Gebauer, in *International Workshop on Position Sensitive Neutron Detectors – Status and Perspectives*, edited by Th. Wilpert and B. Gebauer (Hahn-Meitner-Institut, Berlin, 2001).

[7] Fangwei Wang, (Private Communications, 2005).

[8] N.W. Ashcroft, N.D. Mermin, *Solid State Physics* (Holt, Rinehart and Winston, New York, 1976).

[9] W.H. Tait, *Radiation Detection* (Butterworths, London, 1980).

[10] J.B. Birks, *The Theory and Practice of Scintillation Counting* (Pergamon Press, New York, 1964).

[11] C.W.E van Eijk, A. Bessiére, P. Dorenbos, Nucl. Instrum. Methods A **529**, 260 (2004).

[12] Chart transmitted via email from Frank Yohe, Nichia Corporation.

[13] J.F. Clergeau, B. Guérard, J.C. Buffet, P. Van Esch, *Advances in Neutron Scattering Instrumentation*, Edited by I.S. Anderson and B. Guerard, Proceedings SPIE 4785 (SPIE, Bellingham, Washington, 2002).

[14] G.F Knoll, *Radiation Detection and Measurement*, 3rd ed. (Wiley, New York, 2000).

[15] The data in this plot was obtained from MCNP5

[16] *CRC Handbook of Chemistry and Physics*, 75th ed, Edited by D.R. Lide (CRC Press, Boca Raton, Florida, 1994).

[17] V. Hagopian, I. Daly, *SCIFI 97: Conference on Scintillating Fiber Detectors*, Editors, A.D. Bross, R.C. Ruchti, M.R. Wayne, AIP. Conf. Proc. No. 450 (AIP, New York, 1997).

[18] Chart transmitted via email from Mike Kushner, Saint Gobain Detectors and Crystals, Bicron Division.

[19] Scintillating Fiber Datasheet, Saint Gobain Detectors and Crystals, Bicron Division.

[20] N.J. Rhodes, M.W. Johnson, *Proceedings of the International Conference on Inorganic Scintillators and their Applications*, Edited by P. Dorenbos and C.W.E. van Eijk (Delft University Press, Delft, 1996).

[21] E.M. Schooneveld, J.B. Czirr, T.K. McKnight, N.J. Rhodes, R.M. Ibberson, *Advances in Neutron Scattering Instrumentation*, Edited by I.S. Anderson and B. Guerard, Proceedings SPIE 4785 (SPIE, Bellingham, Washington, 2002), 243.

[22] M.L. Crow, J.P. Hodges, R.G. Cooper, Nucl. Instrum. Methods A **529**, 287 (2004).

[23] R. Stedman, Rev. Sci. Instrum. **30**, 1156 (1960).

[24] P. Thomas, J. Appl. Crystallogr. **5**, 373 (1960).

[25] M.K. Kojima et al., Nucl. Instrum. Methods A **529**, 325 (2004).

[26] Chris Maxwell, (Private Communications, 2005).

[27] RTV Primer Datasheet, GE Silicones.

[28] RTV615 Datasheet, GE Silicones.

[29] *MCNP – A General Monte Carlo N-Particle Transport Code, Version 5*, (Los Alamos National Laboratory, Los Alamose, New Mexico, 2003), Vol. 1.

[30] Neutron Data Booklet, 2nd ed., Edited by A.J. Dianoux and G. Lander, (OCP Science, Philadelphia, 2003).

[31] E. Wilcox, M.S. thesis, Brigham Young University, 2005.

[32] N. Tsoulfanidis, *Measurement and Detection of Radiation*, 2rd ed. (Taylor and Francis, Bristol, Pennsylvania, 1995).

Appendix A

Alpha and Triton Ranges in ZnS and LiF

A.1 – Basic Considerations

Tables and empirical equations exist for determining the range of heavy, charged particles through specified materials. When the approximate range for a particular heavy, charged particle is sought in another material, the Bragg-Kleeman rule may be applied. This rule is stated as,

$$R_1 = \frac{\rho_2}{\rho_1}\sqrt{\frac{A_1}{A_2}}R_2 \tag{A.1}$$

where ρ and A are the density and effective atomic weight for the material designated by the subscript. This rule is most accurate when the effective atomic weights of the two materials are close. The effective atomic weight for a material may be found by,

$$A = \left(\sum_i^L \frac{w_i}{\sqrt{A_i}}\right)^{-2} \tag{A.2}$$

Where i indexes an element in the material and w_i and A_i refers to the weight fraction and atomic weight of an element in a material [32].

When the range of different heavy, charged particles in the same material is desired, an approximate solution is obtained through the relation,

$$R_a(E_a) = \frac{m_a z_b^2}{m_b z_a^2} R_b(E_b = \frac{m_b}{m_a} E_a) \tag{A.3}$$

where R_b is the range given, R_a is the range sought after and m and z are the mass and charge for their respective particle [14].

The range of an alpha particle with energies between 1 to 4 MeV in air is approximated by [32],

$$R(mm) = e^{1.61\sqrt{E(MeV)}} \quad \text{(A.4)}$$

When a $^{6}Li(n,\alpha)^{3}H$ reaction occurs, 4.78 MeV of energy is released with the particles. Due to conservation of momentum, the alpha carries away 2.05 MeV while the triton carries away 2.73 MeV.

The accepted density of air is $1.29x10^{-3}$ gm/cm^3. Table A.1 gives the weight fractions and atomic weights of the majority constituents in air.

Constituent	Oxygen	Nitrogen	Argon
Weight Fraction	0.229	0.745	0.026
Atomic Weight	16.0	14.0	39.9

Table A.1 – Weight fractions and Atomic weights for the constituents of Air.

With these values equation A.2 gives the effective atomic weight of air to be A_{air}=14.7.

A.2 – Alpha and Triton Range in ZnS

The density of ZnS is 4.09 gm/cm^3. Table A.2 gives the weight fractions and atomic weights of the constituents of ZnS.

Constituent	Zinc	Sulfer
Weight Fraction	0.676	0.329
Atomic Weight	65.4	32.1

Table A.2 - Weight fractions and Atomic weights for the constituents of ZnS.

With these values the effective atomic weight of ZnS is found to be A_{ZnS}=50.4.

The range of a 2.05 MeV alpha in air is found by equation A.4 to be 10.03 mm. Using equation A.1, the range of this alpha in ZnS is found to be

$$R_{ZnS_\alpha} = 37.8\ \mu\text{m}$$

The triton has an energy of 2.73 MeV. However, equation A.3 will require an alpha with an energy of,

$$E_\alpha = \frac{m_\alpha}{m_{triton}} E_{triton} = \frac{4}{3} 2.73\ \text{MeV} = 3.64\ \text{MeV}$$

By equation A.4, a 3.64 MeV alpha has a range of 21.58 mm in air. Equation A.1 converts this range in air to 12.6μm in ZnS. Finally, using Equation A.3, the range of a 2.73 MeV triton in ZnS is found to be,

$$R_{zns_{triton}} = \frac{3}{4}\frac{2^2}{1^2} 12.6\ \mu\text{m} = 37.8\ \mu\text{m}$$

A.3 – Alpha and Triton Range in LiF

The density of LiF is 2.64 gm/cm^3. Table A.3 gives the weight fractions and atomic weights of the constituents of LiF.

Constituent	Lithium	Fluorine
Weight Fraction	0.268	0.732
Atomic Weight	6.94	19.0

Table A.3 - Weight fractions and Atomic weights for the constituents of LiF.

With these values the effective atomic weight of LiF is found to be A_{LiF}=13.7.

Again, the range of a 2.05 MeV alpha in air is found by equation A.4 to be 10.03 mm. Using equation A.1, the range of this alpha in LiF is found to be,

$$R_{LiF_\alpha} = 4.7\ \mu\text{m}$$

To determine the range of a 2.73 MeV triton in a material, as shown in section A.2, the range of a 3.64 MeV alpha in air is first needed. This range is 21.58 mm. Equation A.1 converts this range in air to 10.2 μm in LiF. Finally, using Equation A.3, the range of a 2.73 MeV triton in LiF is found to be,

$$R_{zns_{triton}} = 30.6\ \mu\text{m}$$

A.4 – Range Results

Table A.4 restates the results found in sections A.2 and A.3.

Material	Particle energy	Particle Range
ZnS	2.05 MeV alpha	5.9 μm
ZnS	2.73 MeV triton	37.8 μm
LiF	2.05 MeV alpha	4.7 μm
LiF	2.73 MeV triton	30.6 μm

Table A.4 – Summary of Zns and LiF Ranges.

Appendix B

MCNP5 Output Files

The following are MCNP input files for 1 mm round fiber and 1 mm square fiber FEFD prototype calculations and are designed to run on MCNP5. Input files for 2 mm round fiber and 2 mm square fiber FEFD prototype calculations are use similar input file with altered dimensions. The following files were designed for the situation were not attenuation of the photons is assumed in the ZnS/LiF scintillator.

Input file for a FEFD prototype using 1 mm round fibers. The incident neutrons have a wavelength of 1 Å.

```
c
   1     1  -2.42      -1  2  -3  4  -5  6   #2 #3 #4 #5 #6 #7 #8 #9 #10
         #11 #12 #13 #14 #15 #16 #17
   2     1  -2.42      -17 -42 43 35 -36 -3 4 #8
   3     1  -2.42      -18 -42 43 36 -37 -3 4 #9
   4     1  -2.42      -19 -42 43 37 -38 -3 4 #10
   5     1  -2.42      -20 -42 43 -35 39 -3 4 #13
   6     1  -2.42      -21 -42 43 -39 40 -3 4 #14
   7     1  -2.42      -22 -42 43 -40 41 -3 4 #15
   8     2  -1.03      -7  -5  6
   9     2  -1.03      -8  -5  6
  10     2  -1.03      -9  -5  6
  11     2  -1.03      -10  -5  6
  12     2  -1.03      -11  -5  6
  13     2  -1.03      -12  -5  6
  14     2  -1.03      -13  -5  6
  15     2  -1.03      -14  -5  6
  16     2  -1.03      -15  -5  6
  17     2  -1.03      -16  -5  6
  18     0  -34   #1 #2 #3 #4 #5 #6 #7 #8 #9 #10 #11 #12 #13 #14 #15 #16 #17
  19     0  34
  20     0  -29 30 -31 32 -34
```

```
  1       px      1.0
  2       px     -1.0
  3       py      0.1
  4       py     -0.1
  5       pz       5
  6       pz      -5
  7       c/z     0.1   0   0.05
  8       c/z     0.3   0   0.05
  9       c/z     0.5   0   0.05
 10       c/z     0.7   0   0.05
 11       c/z     0.9   0   0.05
 12       c/z    -0.1   0   0.05
 13       c/z    -0.3   0   0.05
 14       c/z    -0.5   0   0.05
 15       c/z    -0.7   0   0.05
 16       c/z    -0.9   0   0.05
 17       c/z     0.1   0   0.17
 18       c/z     0.3   0   0.17
 19       c/z     0.5   0   0.17
 20       c/z    -0.1   0   0.17
 21       c/z    -0.3   0   0.17
 22       c/z    -0.5   0   0.17
 29       px      0.8
 30       px     -0.8
 31       pz      4.8
 32       pz     -4.8
 33       py       10
 34       so      100
 35       px        0
 36       px       .2
 37       px       .4
 38       px       .6
 39       px      -.2
 40       px      -.4
 41       px      -.6
 42       pz        4
 43       pz       -4

mode  n
m1    3007.       -1.39964E-02     $ZnS
      3006.       -2.27995E-01     9019.      -7.58009E-01
      30000.      -2.684008        16000.     -1.315992
      14000.      -.47360250       8016.      -.26972000
      6012.       -.40470875       1001.      -.101968875
m2    6012.        4.85            $plastic fiber
      1001.       4.82
```

```
imp:n  1          17r          0          1          $ 1, 14
tmp1   2.55e-008       19r       $ 1, 14
mt1  benz.60t
mt2  benz.60t
sdef pos=0 10 0 cel=18 erg=8.1803E-8 tme=0 wgt=1
    par=1 sur=33 ccc=20 rad=d1 vec=0 -1 0 dir=1
si1  H 0 4.87
sp1  d -21 1
f4:n (2 3 4 5 6 7)
fm4  -1 1 105
sd4  1.543008882
t4   50 100 200 400 800 1600 3200 6400 12800 25600 51200
e4   0.025E-6 0.05E-6 0.1E-6 0.15E-6 0.2E-6 0.25E-6
    0.30e-6 0.4E-6 1.0E-6 1.0E-4 1.0E-2 1.0 15.0
phys:n 15
thtme 1.0
nps  1000000
dbcn 0 0 0 0 0 0 0 1 0 10 0 0 0 0
print -60 -72 -98 -100 -110 -126 -130 -160 -161 -162
```

Input file for a FEFD prototype using 1 mm square fibers. The incident neutrons have a wavelength of 1 Å.

```
c
   1     1  -2.42      -1  2  -3  4  -5  6  #2 #3 #4 #5 #6 #7 #8 #9 #10 #11 #12
   2     1  -2.42      -3  4  -35 36 -37 38 #5 #6 #7 #8 #9 #10
   3     2  -1.03      15 -16 -5 6 -27 28
   4     2  -1.03      13 -14 -5 6 -27 28
   5     2  -1.03      11 -12 -5 6 -27 28
   6     2  -1.03       9 -10 -5 6 -27 28
   7     2  -1.03       7 -8  -5 6 -27 28
   8     2  -1.03      -17 18 -5 6 -27 28
   9     2  -1.03      -19 20 -5 6 -27 28
  10     2  -1.03      -21 22 -5 6 -27 28
  11     2  -1.03      -23 24 -5 6 -27 28
  12     2  -1.03      -25 26 -5 6 -27 28
  13     0  -34   #1 #2 #3 #4 #5 #6 #7 #8 #9 #10 #11 #12
  14     0  34
  15     0  -29 30 -31 32 -34

   1       px       1.0
   2       px      -1.0
   3       py       0.1
   4       py      -0.1
   5       pz         5
```

```
  6       pz       -5
  7       px      0.05
  8       px      0.15
  9       px      0.25
 10       px      0.35
 11       px      0.45
 12       px      0.55
 13       px      0.65
 14       px      0.75
 15       px      0.85
 16       px      0.95
 17       px     -0.05
 18       px     -0.15
 19       px     -0.25
 20       px     -0.35
 21       px     -0.45
 22       px     -0.55
 23       px     -0.65
 24       px     -0.75
 25       px     -0.85
 26       px     -0.95
 27       py      0.05
 28       py     -0.05
 29       px       0.8
 30       px      -0.8
 31       pz       4.8
 32       pz      -4.8
 33       py        10
 34       so       100
 35       px       0.6
 36       px      -0.6
 37       pz         4
 38       pz        -4

mode  n
m1    3007.        -1.39964E-02     $ZnS/LiF/RTV
      3006.        -2.27995E-01     9019.      -7.58009E-01
      30000.       -2.684008        16000.     -1.315992
      14000.       -.47360250       8016.      -.26972000
      6012.        -.40470875       1001.      -.101968875
m2    6012.         4.85            $plastic fiber
      1001.        4.82
imp:n  1           12r          0           1           $ 1, 14
tmp1   2.55e-008        14r       $ 1, 14
mt1  benz.60t
mt2  benz.60t
```

```
sdef pos=0 10 0 cel=13 erg=8.1803E-8 tme=0 wgt=1
    par=1 sur=33 ccc=15 rad=d1 vec=0 -1 0 dir=1
si1  H 0 4.87
sp1  d -21 1
f4:n 2
fm4  -1 1 105
t4   50 100 200 400 800 1600 3200 6400 12800 25600 51200
e4   0.025E-6 0.05E-6 0.1E-6 0.15E-6 0.2E-6 0.25E-6
    0.30e-6 0.4E-6 1.0E-6 1.0E-4 1.0E-2 1.0 15.0
phys:n 15
thtme 1.0
nps  1000000
dbcn 0 0 0 0 0 0 0 1 0 10 0 0 0 0
print -60 -72 -98 -100 -110 -126 -130 -160 -161 -162
```